TECHNISCHE UNIVERSITÄT WIEN

Degree in
Mechanical engineering

Atmospheric angular momentum budget in idealized general circulation simulation

Gaëlle LELOUP

BOARD MEMBERS

-	Committee member
Prof. Alfredo Soldati	Supervisor
Prof. Francesco Zonta	Co-Supervisor

Author's e-mail:
gaelle.leloup@lsce.ipsl.fr

Acknowledgments

I would like to thank several people that helped me during this master thesis. First, I would like to thank my two supervisors from TU Wien, F. Zonta and A. Soldati, who have accepted to supervise me and be part of my committee for this master thesis topic which is quite different from the usual fields of TU Wien. This allowed me to discover the field of climate modeling, in which I have decided to continue in the next years. I had the chance to be hosted at two french laboratories : LMD (Laboratoire de Météorologie Dynamique) and LSCE (Laboratoire des Sciences du Climat et de l'Environnement) and supervised there by T. Dubos and S. Fromang. Thank you for your supervision, helpful comments and feedbacks. I especially thank the whole LSCE CLIM (Climate Modeling) team : thank you for your help and sympathy, that have convinced me to stay with you in the next 3 years.

Abstract

In this thesis, simulations of the general circulation of idealized Earth and Venus atmosphere with the newly developed dynamical core DYNAMICO are carried out. Its angular momentum budget is investigated. Numerical models solving the Navier-Stokes equations may have purely numerical, spurious sources of angular momentum. The magnitude of these terms must be small in comparison to the physical terms of the budget for the simulations to be credible.
In the case of the idealized Earth configuration, the angular momentum budget of DYNAMICO was found to be satisfying. However, the situation is more complex on Venus, where it is not easily possible to evaluate the impact of the numerical errors on the global circulation obtained.

Contents

1 Introduction

The modeling of the atmosphere is a key part in climate modeling, and an accurate description of an atmosphere requires an accurate description of its angular momentum balance. This is even more the case on planets like Venus, which are superrotating.

The total angular momentum of a planet and its atmosphere is conserved, as there are no external torques acting. Exchange of angular momentum are taking place between the solid planet (or oceans) and the atmosphere, due to frictional and mountain torques (physical torques).

However, numerical model may have numerical, spurious sources or sinks of Angular Momentum (AM). These numerical torques have to be small in comparison to the physical torques applied, to obtain reliable simulation results.

During this master thesis, I was hosted by the french laboratories Laboratoire de Météorologie Dynamique (LMD), and Laboratoire des Sciences du Climat et de l'Environnement (LSCE), and supervized there by T. Dubos and S. Fromang. LMD and LSCE have developed a new General Circulation Model (GCM) for the atmosphere : DYNAMICO. It conserves exactly mass, vorticity and energy but not AM. The main goal of this thesis was to check the quality of the AM budget of this new Atmospheric General Circulation Model ($AGCM$).

The master thesis is divided as follow : in a first part, we give general informations on climate modeling and more specifically informations on the GCM considered during this study, DYNAMICO. We also define the atmospheric angular momentum and the method used to check the quality of the angular momentum budget in the GCM. The second and third parts present the study of two idealized atmospheres : an idealized configuration for the Earth (the Held Suarez test case) in the second part and an idealized configuration for Venus (often referred to in the literature as the "ISSI configuration") in the third part.

1.1 Climate modeling

1.1.1 Context and climate models

The Institut Pierre et Simon Laplace ($IPSL$) is an organization of laboratories working on climate and environment. Numerical models of components of the climate system are being developed in the different laboratories : there are models for the atmosphere, the oceans, continental surfaces, sea ice, marine and terrestrial ecosystems, atmospheric chemistry. Physical, chemical and biogeochemical processes are also considered. Coupled together, these different model components allow to model the interactions taking place between the different parts of the climatic system. A climate model is used to study the natural variability of climate, its past and future changes, as well as its response and sensitivity to anthropogenic forcing.

A General Circulation Model (GCM) is a type of climate model used to represent the general circulation of the atmosphere or ocean of a planet. Atmospheric General Circulation Models (AGCM) are of key importance in climate modeling and can be used either alone or coupled to the other model components. The current version of the IPSL climate model uses the Atmospheric GCM LMDZ (developed at LMD since the seventies) for the atmospheric component.

DYNAMICO is a new Atmospheric General Circulation Model (AGCM) being developed at LMD and LSCE, able to run on more cores simultaneously (and therefore, faster) than LMDZ.

1.1.2 Atmospheric General Circulation Model : parametrizations and dynamical core

Atmospheric GCM are used to compute the evolution of a planetary atmosphere by taking into account physical processes (clouds, humidity, radiative processes etc). The relevant fields (like velocity, temperature) are evolved with time by solving the governing equations.
To do so, the atmosphere is meshed and divided into cells and the governing equations are solved using numerical methods, which differ according to the atmospheric GCM used. Common methods are spectral, finite volume or finite element methods.
All processes involved cannot be resolved, as it would require an enormous computation time. Only the processes having a larger length scale than the grid cells can be resolved. However, one still has to account for smaller, sub-grid scale processes : they have to be parametrized.
An atmospheric GCM is therfore divided into two components : the parametrizations and the dynamical core.

- The **parametrizations** (the **physical parametrizations**) account for the modeling of the physical and sub-grid scale processes : it approximates the radiative processes, phase changes, or water processes, like clouds or precipitations through a statistical description. The parametrizations also take into account the orography (pressure differences accross mountains affect the general circulation). These parametrizations are not fixed in time and depend on the general circulation.
- The **dynamical core** is the resolved, fluid flow component of a GCM : it solves the governing equations on the grid through time (the **dynamics**). However, as the governing equations for the flow are non linear, energy cascades through the resolved scale to scales smaller than the grid (unresolved scales). In reality, these processes would cascade to smaller and smaller scales until the dissipation length scale at which they would be dissipated by friction. Due to computation time restriction, one cannot have grid cells small enough to model these processes and the dissipation length scale is smaller than the one being resolved with the model. In GCM, energy can accumulate at the truncation limit due to these processes, that would make the simulation unstable. To avoid this, artificial dissipation is added through the use of 2nd or 4th order diffusion operator that act on momentum and temperature (the **dissipation**).

These two components, the physical parametrizations and the dynamical core (which includes the dynamics and the dissipation) are coupled. The dynamical core calculates the evolution of the wind velocity field, temperature, and calculates the transport of different variables, called tracers (like water in its different forms, or chemical components). The dynamical core is forced by the physical parametrizations, which strongly depends on the tracers. This is schematized in Fig. 1.1.
To obtain a realistic simulation, a functional dynamical core solving the governing equations correctly is a key element. The focus of the thesis was set on the study and validation of the dynamical core of the atmospheric GCM and not on the parametrizations. However, for a simulation to be realistic, the physical processes should also be parametrized in a realistic way. For example, in the case of the modeling of the Earth's atmosphere for future climate predictions, the critic is often made that the parametrizations are not satisfying, especially in the modeling of clouds.
The validation of dynamical core is often made by seeing it as a dry dynamical process : the phase changes of water and transport of tracers are not included. Parametrization are simplified, to have a "simplified physics", on which the dynamical core is tested.
During this thesis, modeling of the atmosphere of the Earth and Venus was performed, with simplified physical parametrizations, described in Section 2.2 in the case of the Earth and in Section 3.2 in the case of Venus.

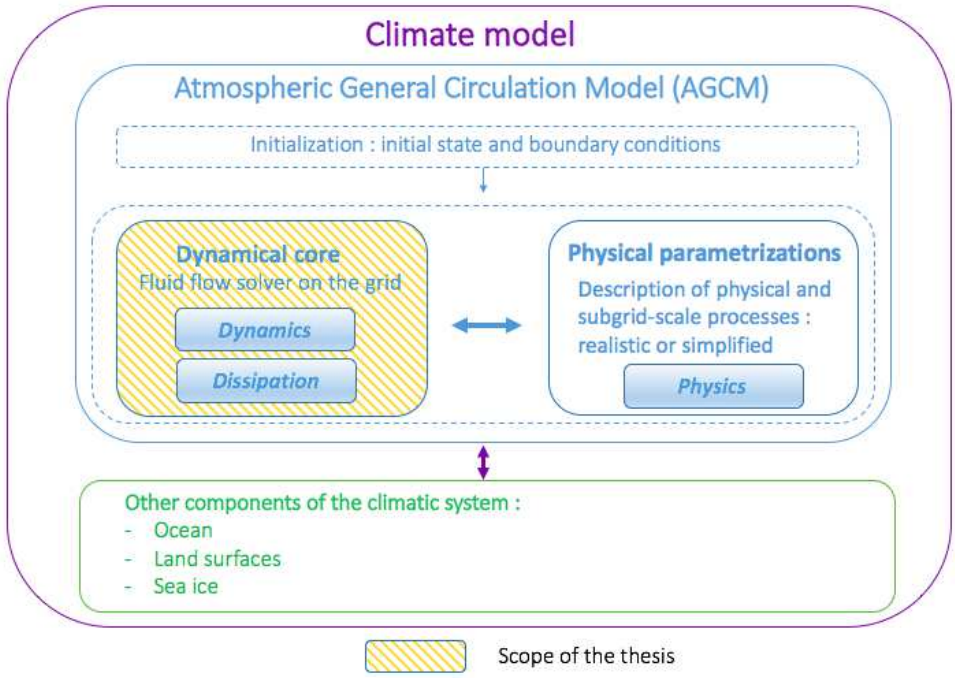

FIGURE 1.1 – Schematic representation of a climate model

To make the different fields evolve with time, the dynamical core has to take into accounts the three interconnected processes :

- the physics
- the dissipation
- the dynamics

Time - splitting is used and these three processes are taken into account one after another, as schematized in Fig. 1.2. The dynamics is called at every timestep, as this is the process making every variable field evolve with time. The physics and dissipation processes are not necessarily called at every timestep, as their characteristic timescales are usually longer.

1.1.3 Details on the dissipation

In GCM, there can be different types of dissipation ([15], [14]):

- **Physical diffusion** is present in the atmosphere, caused by turbulence. This feature is too small to be represented explicitely and needs to be parametrized in a realistic way in the physical parametrizations.
- Non physical diffusion (or filter, scale selective process) is added in atmospheric models explicitely to avoid the accumulation of shortwave energy at the truncation limit (short waves that would cascade to smaller length scales in a physical process), with the use of **explicit diffusion operators**.
- There is also **internal dissipation** due to the discretization scheme, like for example when using finite differences.
- The use of a **sponge layer** is also sometimes considered as part of the dissipation process. A sponge layer is an artefact to avoid wave reflection on the model top.

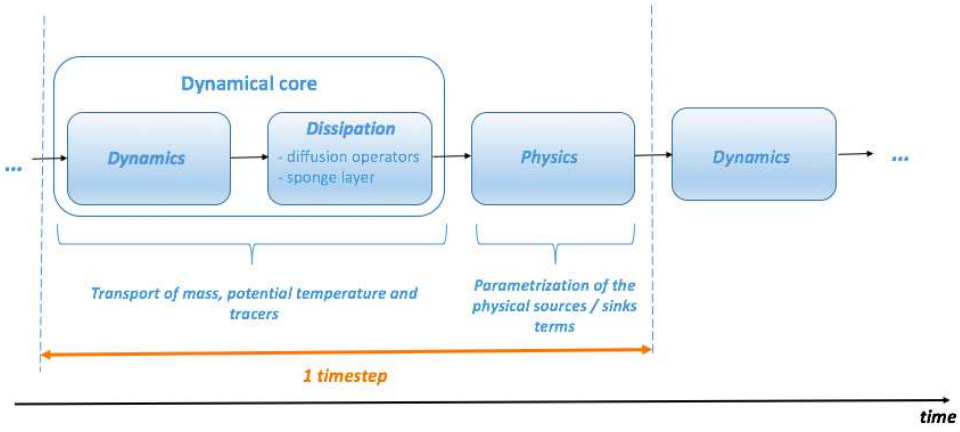

FIGURE 1.2 – Schematic representation of the time splitting process. The dynamics, dissipation and physics are called one after another. The dynamics is called at every timestep, while the physics and dissipation are not necesserely called at every timesteps, but every few timesteps.

The difficulty when using explicit diffusion operator is to perform a sufficient damping of the non physical processes and shorter wavelength, while keeping the higher wavelength undamped. Such a scale selective process is usually performed by an iterated laplacian, added explicitely to the right side of the equation :

$$\frac{\partial h}{\partial t} = (-1)^{q+1} K \nabla^{2q} h \tag{1.1}$$

with h representing any variable, K the diffusion coefficient, and q the order of the iterated Laplacian. When q is higher than zero, this process is scale selective. Usually, q is taken equal to 1 or 2 (second or fourth order laplacian). A fourth order Laplacian is more scale selective than a second order one.

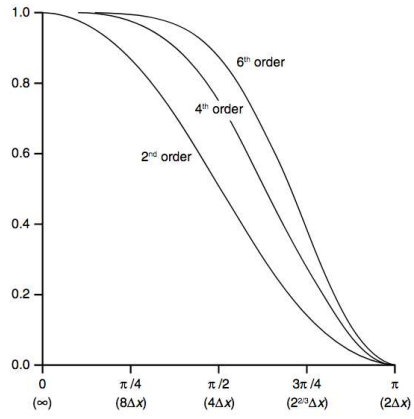

FIGURE 1.3 – Schematic representation of the scale selectivity of iterated laplacians. Picture from [15]. The x-axis represents the scale of the motion : infinite on the left extremity and of the grid cell on the right extremity. The y-axis represents an amplitude : processes of a smaller length scale than the grid scale are completely damped, whereas processes of large length scale are undamped. When the order of the Laplacian is increased, the process becomes more scale selective, and only the length scales close to the grid scale are damped, while the other remain undamped.

This is represented schematically on Fig. 1.3 : For large scale waves (left side of the graph), no damping is performed, while scales smaller than the grid size (right side of the graph) are

cut of. One can see that depending on the Laplacian order, the intermediate scales are more or less affected. The higher the order of the Laplacian, the less the intermediate scales are affected (only the small scales are damped). For a second order Laplacian, one can see that the medium scales are strongly affected by this damping process.
From a scale analysis of eq. (1.1), one obtains :

$$K \approx \frac{l^{2q}}{\tau_d} \tag{1.2}$$

with K the equivalent dissipation coefficient, l the grid length scale and τ_d the characteristic timescale for the dissipation.

1.1.4 Differences between LMDZ and DYNAMICO

DYNAMICO is a new dynamical core, that is being developped at LMD and LSCE and will likely replace in the future the current AGCM of IPSL, LMDZ.
There are several differences between the dynamical core LMDZ and DYNAMICO. The current LMDZ dynamical core is based on a latitude-longitude grid (schematized in Fig. 1.4) and uses finite-difference methods.
One of the major problems of this method is the convergence of the meridians at the pole, known as the "pole problem".
Indeed, finite difference schemes have a restriction on the timestep. This is known as the Courant Friedrich Levy (CFL) condition, which imposes :

$$\frac{u\delta t}{\delta x} \leq C_{max} \tag{1.3}$$

with δx being the grid interval, u being the wind velocity and δt being the time step.
On a latitude-longitude grid, the longitudinal grid interval decreases at the pole, and a shorter time step is needed to reach stability, which increases the computation time. A polar filter is usually used to overcome this difficulty. However, with the use of a polar filter it is not possible to divide the computational load longitudinally, but only according to latitude and vertical level. Such problem does not exist in DYNAMICO, as each cell is approximately of the same size. It is possible to share the computational load more efficiently, longitudinally, latitudinally and according to vertical levels.
For example, for resolutions equivalent to $1^\circ \times 2^\circ$, LMDZ can be run on 30 cores simultaneously, whereas DYNAMICO can be run on 90 cores. For higher resolutions, the comparative advantage of DYNAMICO becomes even stronger.
As it can be run on more core simultaneously, DYNAMICO allows to realize simulations faster.

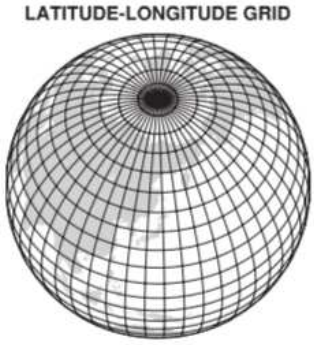

FIGURE 1.4 – Longitude latitude grid. Picture from [25].

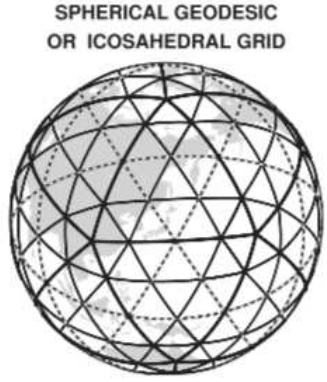

FIGURE 1.5 – Icosahedral grid (quasi-uniform). Picture from [25].

1.2 The dynamical core DYNAMICO

1.2.1 Equations solved

Equation set

AGCM are based on the resolution of several equations :

- the continuity equation, eq. (1.4)
- the momentum (Navier - Stokes), eq. (1.5) in a simplified form, detailed in the following section.
- the energy conservation equation, eq. (1.6)
- the ideal gas law, eq. (1.7)
- equations for the conservation of chemical species (tracers), eq. (1.8)

For simplicity, the fluid is here assumed to be of a single phase and of fixed composition. The governing equations for a compressible fluid in a reference frame rotating with angular velocity $\mathbf{\Omega}$ (s^{-1}) may be written as [14] :

$$\frac{\partial \rho}{\partial t} + \nabla \cdot (\rho \mathbf{u}) = 0 \tag{1.4}$$

$$\frac{Du}{Dt} + 2\mathbf{\Omega} \times \mathbf{u} + \frac{1}{\rho}\nabla p + \nabla \Phi = \mathbf{F} \tag{1.5}$$

$$\frac{D\Theta}{Dt} = S_\theta \tag{1.6}$$

$$p = RT\rho \tag{1.7}$$

$$\frac{Dq}{Dt} = S_q \tag{1.8}$$

In this equation set :

- $\mathbf{\Omega}$ is the planetary rotation vector. On Earth, $\Omega = 7.27 \cdot 10^{-5} s^{-1}$, and on Venus $\Omega = 2.99 \cdot 10^{-7} s^{-1}$. Venus is rotating much slower than the Earth.
- ρ is the fluid density in $kg \cdot m^{-3}$
- $\mathbf{u}$ is the fluid velocity vector in the rotating reference frame (the planetary reference frame) in $m \cdot s^{-1}$
- T is the temperature, in K
- Θ is the potential temperature, with $\Theta = T(\frac{p_0}{p})^{\frac{R}{C_p}}$, in K
- R is the gas constant for dry air, $R = \frac{R_m}{M}$ with R_m the universal gas constant, $R_m = 8,314\ J \cdot mol^{-1} \cdot K^{-1}$ and M the molar mass of dry air ($kg \cdot mol^{-1}$). For the Earth atmosphere, $M = 28.966 \cdot 10^{-3} kg \cdot mol^{-1}$, and $R = 2870.2\ J \cdot K^{-1} \cdot kg^{-1} (m^2 \cdot s^{-2} \cdot K^{-1})$. For Venus atmosphere, $M = 43.4 \cdot 10^{-3} kg \cdot mol^{-1}$, and $R = 191.4 J \cdot K^{-1} \cdot kg^{-1} (m^2 \cdot s^{-2} \cdot K^{-1})$.
- p is the pressure and p_0 is a reference pressure.
- C_p is the specific heat capacity at constant pressure, in $J \cdot K^{-1} \cdot kg^{-1}$
- Φ is the modified gravitational potential. The centrifugal term $\mathbf{\Omega} \times (\mathbf{\Omega} \times \mathbf{r})$ is accounted in Φ : the centrifugal term derives from a potential and is then combined with the gravitational potential to form the modified gravitational potential.

$$\nabla \Phi = \mathbf{g} - \mathbf{\Omega} \times (\mathbf{\Omega} \times \mathbf{r}) = \mathbf{g}'$$

$$\Phi = gz - \frac{\Omega^2 r^2}{2}$$

with r the distance to the planet axis ($r = acos(\phi)$, with a being the planetary radius) and z the altitude from the planet surface, g the surface gravity field (g = 9.81 $m \cdot s^{-2}$ on Earth and g = 8.87 $m \cdot s^{-2}$ on Venus).

- S_θ and S_q represent source or sink terms. These terms can be linked to explicit processes (like phase change processes, chemical reactions) and subgrid scale processes. They are parametrized in the physical part of the GCM.
- **F** is the friction term.

Explicit diffusion operators are added to the equations eq. (1.5) and eq. (1.6) in order to avoid energy accumulation at the truncation level and numerical instability.

The hydrostatic primitive equations

Most of the climate models do not use the complete Navier-Stokes equations, but rather a simplified version. This is of interest, as they are usually easier to solve. The most commonly used equation set is called the Hydrostatic Primitive Equations (HPE). DYNAMICO solves the Hydrostatic Primitive Equations.
A spherical coordinate system (represented in Fig. 1.6) is used to describe the motion. The relative velocity of the air is described in this coordinate system by :

$$\overrightarrow{v} = u\overrightarrow{e_\lambda} + v\overrightarrow{e_\phi} + w\overrightarrow{e_r} = \begin{pmatrix} w \\ u \\ v \end{pmatrix}_{(\overrightarrow{e_r},\overrightarrow{e_\lambda},\overrightarrow{e_\phi})} \tag{1.9}$$

$$\begin{cases} u = rcos(\phi)\frac{d\lambda}{dt} \\ v = r\frac{d\phi}{dt} \\ w = \frac{dr}{dt} \end{cases} \tag{1.10}$$

with λ being the longitude, going from -180° to +180° , ϕ being the latitude, going from -90° (south pole) to +90° (North pole), and r being the distance to the planet center. u is the **zonal component** of the wind (east-west component), v is the **meridional component** of the wind (north-south component), and w is the **vertical component** of the wind (ascending or descending motions).

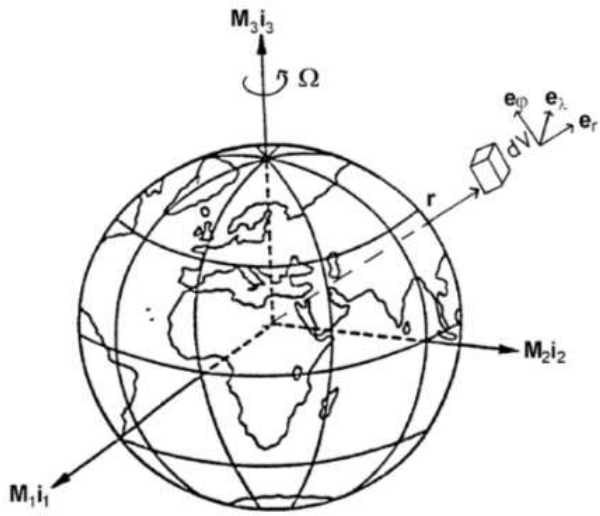

FIGURE 1.6 – Spherical coordinates. Picture from [6]

The momentum equation (in its non-simplified form) can be written in spherical coordinates as :

$$\begin{cases} \frac{Du}{dt} - 2\Omega v sin(\phi) + 2\Omega w cos(\phi) + \frac{uw}{r} - \frac{uvtan(\phi)}{r} = -\frac{1}{\rho r cos(\phi)} \frac{\partial p}{\partial \lambda} + F_r \\ \frac{Dv}{dt} + 2\Omega u sin(\phi) + \frac{vw}{r} + \frac{u^2 tan(\phi)}{r} = -\frac{1}{\rho r} \frac{\partial p}{\partial \phi} + F_\phi \\ \frac{Dw}{dt} - 2\Omega u cos(\phi) - \frac{u^2+v^2}{r} = -\frac{1}{\rho} \frac{\partial p}{\partial r} - g + F_\lambda \end{cases} \tag{1.11}$$

To obtain the HPE form used in GCM, several approximation are made : (detailed in [4])

- The spherical geopotential approximation is made. The geopotential are surfaces of constant Φ. These geopotential surfaces are not spherical. However, the departure from sphericity is sufficiently small to approximate it as spherical geopotential [4]. The surfaces of constant geopotential are defined by the height $z*$, $z^* = z + \frac{\Omega^2 a^2 cos(\phi)}{2g}$. As $\frac{\Omega^2 a^2 cos(\phi)}{2g} \approx 11km$ at the equator (Earth case), which represents approximately 0.2 % of the Earth's radius, one can approximate that the geopotential surfaces are spherical, as schematized in Fig. 1.7. In the case of Venus, this approximation is even more verified as $\frac{\Omega^2 a^2 cos(\phi)}{2g} \approx 0.2\ km$ at the equator, representing 0.003 % of the planetary radius.

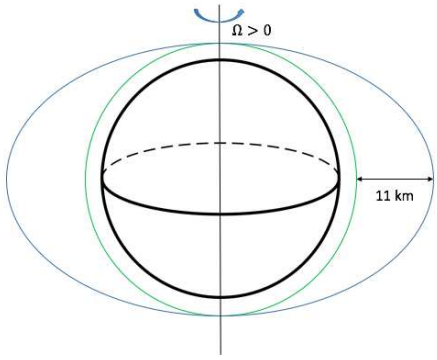

FIGURE 1.7 – Surfaces of constant altitude z are schematized by the green circle, surfaces of constant geopotential, $z^* = z + \frac{\Omega^2 a^2 cos(\phi)}{2g}$ are schematized by the blue ellipse. The excentricity of the blue ellipse is exagerated : it is almost spherical.

- The shallow atmosphere approximation is made. The atmosphere height is small in comparison to the planetary radius : in the case of the Earth, 99.9 % of its mass lies in the first 50 km, and in the first 65km in the case of Venus, corresponding to approximately 1% of the planetary radius in both cases. Therefore, the distance r from a point in the atmosphere to the planet center can be replaced by a (planetary radius) in the equation and $\frac{\partial}{\partial r}$ can be replaced by $\frac{\partial}{\partial z}$ with z the height above sea level.
- The Coriolis term approximation is made. The Coriolis force is defined in the spherical coordinate system by :

$$\overrightarrow{F_c} = 2\mathbf{\Omega} \times \mathbf{U} = 2\Omega \begin{pmatrix} -ucos(\phi) \\ wcos(\phi) - vsin(\phi) \\ usin(\phi) \end{pmatrix}_{(\overrightarrow{e_r}, \overrightarrow{e_\lambda}, \overrightarrow{e_\phi})} \tag{1.12}$$

One can make two approximations. As the vertical component ($\cdot\overrightarrow{e_r}$) competes with gravity and is much smaller, it can be neglected. Furthermore, as one can see in Fig. 1.8, due to the thinness of the atmosphere, vertical motions w are much smaller than horizontal ones (u and v). On Earth, the characteristic scales are 10 $m \cdot s^{-1}$ for horizontal motions and 0.01 $m \cdot s^{-1}$ for vertical ones (3 order of magnitude of difference). On Venus, the characteristic scales are 10 $m \cdot s^{-1}$ for horizontal motions and 1 $m \cdot s^{-1}$ for vertical ones

(1 order of magnitude of difference). Therefore, one can drop the $wcos(\phi)$ term in the Coriolis force. This leads to :

$$\overrightarrow{F_c} \approx 2\Omega \begin{pmatrix} 0 \\ -vsin(\phi) \\ usin(\phi) \end{pmatrix}_{(\overrightarrow{e_r},\overrightarrow{e_\lambda},\overrightarrow{e_\phi})} = 2f\hat{\mathbf{z}} \times \mathbf{U} \tag{1.13}$$

with $\hat{\mathbf{z}}$ the vertical vector directed along $\mathbf{\Omega}$ ($\hat{\mathbf{z}} = i_3$ on Fig. 1.6). The Coriolis parameter is defined by $f = 2\Omega sin(\phi)$

- The hydrostatic approximation is made. On the vertical component of the momentum equation, all terms apart from the pressure and gravity terms can be neglected as they are much smaller. This leads to the **hydrostatic balance** :

$$\frac{\partial p}{\partial z} = -\rho g \tag{1.14}$$

- As the vertical motions w are much smaller than horizontal ones, terms involving w can be, as a first approximation, be neglected.
- The friction term $\mathbf{F}$ is negligible for all scale of motions except the smallest scale turbulent motions near the ground. This term is negligible in the scale of motion solved by the dynamical core : $\mathbf{F} = 0$. It needs to be parametrized.

Scale	*Symbol*	*Venus*	*Earth*
Vertical scale	H	15.9 km $\approx 10^4$ m	~ 10 km
Zonal velocity	U	~ 100 m s^{-1}	~ 10 m s^{-1}
Meridional velocity	V	~ 10 m s^{-1}	~ 10 m s^{-1}
Vertical velocity	W	$\lesssim$ 1 m s^{-1}	~ 1 cm s^{-1}
Radius	a	~ 6.0×10^6 m	~ 6.0×10^6 m
Rotation rate	Ω	2.99×10^{-7} rad s^{-1}	7.29×10^{-5} rad s^{-1}
Acceleration of gravity	g	8.8 m s^{-2}	9.81 m s^{-2}
Timescale	T	~ 10^6 s	~ 10^5 s

Term in eq. (3.2) – (3.4)	*Venus* (m s^{-2})	*Earth* (m s^{-2})
$\frac{u^2}{a}$	10^{-3}	10^{-5}
$2\Omega u \cos\phi$	10^{-5}	10^{-3}
$\frac{Du}{Dt}$	10^{-4}	10^{-4}
$\frac{u^2 \tan\phi}{r}$	10^{-3}	10^{-5}
$2\Omega u \sin\phi$	10^{-5}	10^{-3}
$-\frac{1}{\rho}\frac{\partial p}{\partial y}$	10^{-3}	10^{-3}
$\mathbf{F}_r$	10^{-12}	10^{-12}

FIGURE 1.8 – Characteristic length scales for Venus and Earth atmosphere. Pictures from [16]

The hydrostatic primitive equations are :

$$\begin{cases} \frac{Du}{dt} - fv - \frac{uvtan(\phi)}{r} = -\frac{1}{\rho r cos(\phi)}\frac{\partial p}{\partial \lambda} \\ \frac{Dv}{dt} + fu + \frac{u^2 tan(\phi)}{r} = -\frac{1}{\rho r}\frac{\partial p}{\partial \phi} \\ 0 = \frac{\partial p}{\partial z} + \rho g \end{cases} \tag{1.15}$$

with $f = 2\Omega sin(\phi)$
In the case of the Earth and Venus atmosphere, this leads to different kind of balance, as the terms have different orders of magnitude.

- In the case of large scale atmospheric motions of quickly rotating planets like the Earth, the dominant balance is the **geostrophic balance** : the pressure forces are balanced by the Coriolis force.

$$\begin{cases} -fv = -\frac{1}{\rho r cos(\phi)}\frac{\partial p}{\partial \lambda} \\ fu = -\frac{1}{\rho r}\frac{\partial p}{\partial \phi} \end{cases} \tag{1.16}$$

- In the case of slowly rotating planet like Venus, the dominant balance is the **cyclostrophic balance** : the equatorward component of the centrifugal force balances the meridional pressure gradient force [16].

$$\frac{u^2 tan(\phi)}{r} = -\frac{1}{\rho r}\frac{\partial p}{\partial \phi} = -\frac{1}{\rho}\frac{\partial p}{\partial y} \tag{1.17}$$

1.2.2 Mesh and solver

Horizontal mesh

DYNAMICO is an icosahedral dynamical core : the mesh is based on the subdivision of the twenty triangles of an icosahedron (see Fig. 1.9). These triangles are then divided into smaller triangles, until a satisfying resolution is reached. These subdivisions are quantified by the parameter nbp. Hexagonal cells are obtained by the use of a Voronoi diagram (see Fig. 1.10). There are 10 nbp^2 + 2 cells $\approx 10nbp^2$.

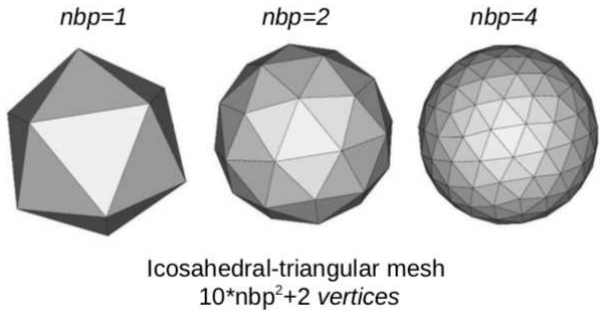

FIGURE 1.9 – Representation of the subdivision of the icosahedron. npb represents the amount of subdivisions. Picture from [2]

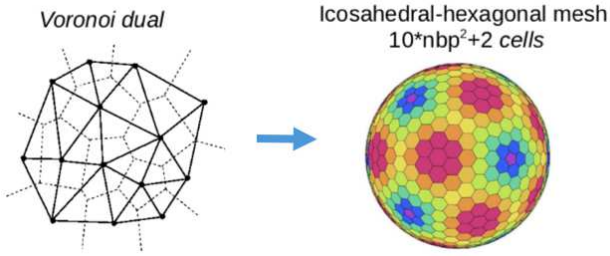

FIGURE 1.10 – Representation of the subdivision of the mesh, obtained from the Voronoi dual. Picture from [2]

As one increases the parameter nbp, the characteristic length scale of an hexagonal cell decreases, and the resolution increases. One can calculate the characteristic length scale of an hexagonal cell with the formula :

$$10nbp^2 \cdot l^2 \approx \underbrace{4\pi a^2}_{planetary\ surface} \tag{1.18}$$

with a the planetary radius. Therefore,

$$l \approx \sqrt{\frac{4\pi}{10}} \frac{a}{nbp} \tag{1.19}$$

In longitude - latitude grids, due to the convergence of the meridians at the pole, and the need to use polar filters, it is impossible to share efficiently the computational load among many cores. The major interest of quasi-uniform grids therefore lies in the possibility to avoid this computational bottleneck, because the grid does not have any singular point, and the load can be shared efficiently among several cores.

Vertical mesh

The grid is also divided in a series of vertical levels, defined by pressure levels. The levels used by DYNAMICO are hybrid-pressure levels. The vertical levels are defined by :

$$P(time, lev, lat, lon) = a(lev) + b(lev) \cdot P_s(time, lat, lon) \tag{1.20}$$

with P the pressure at a certain time and location (at a certain latitude, longitude and vertical level), P_s the surface pressure at a certain time and location (latitude and longitude) and a and b coefficients depending on the level. The pressure at each level therefore depends on the surface pressure. In the levels near the ground, the influence of the surface pressure is strong. However, in the top vertical levels, there is almost no influence of the surface pressure anymore and levels are defined by a fixed pressure (the coefficient b tends toward zero). This is schematized in Fig. 1.11.
The amount of vertical levels is called llm.

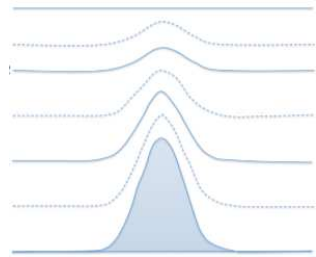

FIGURE 1.11 – Picture from [5] : vertical levels in Dynamico. The levels near the ground are influenced by the surface pressure while the one near the top are at constant pressure

Numerical solver

The Dynamical core DYNAMICO uses a finite volume scheme for the transport of mass, potential temperature and tracers. The discretization of the momentum budget is performed using finite difference like method, and the time integration is performed using Runge-Kutta like schemes. All the numerical aspects are detailed in [5].

1.2.3 Inputs

There are several parameters that one can change before launching a simulation :

- The **initial state**. One can start from different initial state. During this thesis, only simulation starting from rest ($\mathbf{u} = 0$), or from another simulation performed were considered. But it is also possible to start simulations from arbitrarily defined fields.
- The **physical package**, ie the choice of what will be contained in the physical parametrizations. It defines if the atmosphere considered will be an Earth-like, or Venus-like atmosphere, and whether water cycle, chemical species are included or not. During this thesis, the physical packages used are simplified ones, corresponding to the test cases described in Section 2.2 in the case of the Earth and in Section 3.2 in the case of Venus.
- The **boundary conditions**. At the top of the atmosphere, one often uses a **"sponge layer"** boundary condition. The role of the sponge is to avoid wave reflection at the model top. To do so, the winds are damped to zero on the last levels of the model. One can choose the amount of levels included in the sponge (usually the last 3 or 4 vertical levels), as well as the relaxation time (time needed to relax the winds toward zero). The wind variations due to the sponge layer are :

$$\left(\frac{du}{dt}\right)_{Sp} = \begin{cases} -k_{Sp}(p) \cdot u & for\ the\ 3\ or\ 4\ top\ levels \\ 0\ elsewhere\ (k_{Sp}(p) = 0) \end{cases} \tag{1.21}$$

$k_{Sp}(p)$ is the relaxation coefficient, depending on pressure, $k_{Sp}(p) = \frac{1}{t_{sp}}(p)$ with t_{sp} the relaxation time. $k_{Sp}(p) = 0$ everywhere except at the 3 or 4 top levels (the wind damping is only performed at the model top). The sponge layer is part of the dissipation process in DYNAMICO. During this thesis, simulation with or without sponge layer were carried out.

- The parameters of the **explicit diffusion operators**, mentioned in Section 1.1. One can choose the order of the diffusion operator applied, as well as the characteristic diffusion timescale. Different diffusion operators are applied to the potential temperature, the divergent and non divergent parts of the wind : one therefore has to specify the order and timescale of these 3 dissipation operators.
- The **resolution**. One can specify the horizontal resolution of the simulation, by choosing the value of nbp as well as the vertical resolution, by choosing the amount of vertical levels llm.
- Various constants can be changed, like the rotation rate of the planet Ω, the gravity constant g, the planetary radius R and so on.

1.2.4 Outputs

The different parameters of the general circulation are computed on the icosahedral cells of the mesh. These value are then interpolated on a latitude longitude grid, in order to facilitate the results post-processing. The variables of importance considered during this work were the pressure (P), the horizontal wind velocity (zonal component u and meridional component v), the vertical wind velocity (w) and the temperature (T).
These variables are given as outputs in 4D matrices : depending on the time, the vertical level, the latitude and the longitude. The size of the output data is consequent. For one computational timestep, one has to store $llm \cdot lat \cdot lon$ numbers per data : with llm being the amount of vertical levels (40 to 80 depending on the simulations), lat being the size of the discretization over latitude (usually 90 meaning that the data are interpolated on a 2 $^\circ$ latitude grid), and lon being the size of the discretization over longitude (usually 180, meaning that the data are interpolated on a 2 $^\circ$ longitude grid).
Therefore, one cannot store the data at all timesteps. It has to be often enough in order not to loose information, and seldom enough to limit the amount of data stored. For Earth simulations, data were stored one time per day, and for Venus simulations, data were stored 4 time per Venus day (1 Venus day = 117 Earth days).

1.2.5 Resolution

As mentioned previously, one can choose the vertical and horizontal resolution of the mesh by choosing the amount of vertical levels llm and the amount of nbp for the horizontal resolution. However, improving the resolution has a strong numerical cost. Indeed, to have mesh cells smaller by a factor of two, one has to multiply the parameter nbp by two. This multiplies the amount of grid cells by four, as there are $10nbp^2$ cells horizontally. In order to satisfy the CFL condition for the time integration with two times smaller cell, one has to divide the integration timestep by two. This leads to an overall multiplication by 8 of the computational cost. The computational cost increases with a power of 3 relative to the horizontal resolution.
Therefore, one is limited in the horizontal resolution used, especially in the case of Venus, where the simulations are quite long.

1.3 Atmospheric Angular Momentum

1.3.1 General definition

The global angular momentum of an atmosphere is an important characteristic of its rotational inertia, reflecting at the same time the rotation due to the Earth's rotation and the rotation due

to the winds [6].
The angular momentum per unit volume is defined as :

$$\overrightarrow{m} = \rho \overrightarrow{r} \wedge (\overrightarrow{v} + \overrightarrow{\Omega} \wedge \overrightarrow{r}) \tag{1.22}$$

where $\overrightarrow{r}$ is the position vector, $\overrightarrow{\Omega}$ is the angular velocity vector of the Earth, $\overrightarrow{v}$ is the relative velocity of the the air with respect to the rotation of the Earth.
The total atmospheric angular momentum is the integral of the angular momentum per unit volume over the volume V of the Earth's atmosphere.

$$\overrightarrow{M} = \int_V \overrightarrow{m} dV \tag{1.23}$$

It can be decomposed into 3 components, following the 3 main axis (see Fig. 1.6):

- the axial component (Axial Angular Momentum, AAM) along the axis of rotation, $m_3 = \overrightarrow{m} \cdot \overrightarrow{i_3}$ with $\overrightarrow{i_3}$ the basis vector in the direction of the Earth's rotational axis.
- 2 equatorial components, in the equatorial plane

The axial angular momentum per unit volume is therefore :

$$m_3 = \overrightarrow{m} \cdot \overrightarrow{i_3} = \rho \overrightarrow{r} \wedge (\overrightarrow{v} + \overrightarrow{\Omega} \wedge \overrightarrow{r}) \cdot \overrightarrow{i_3} \tag{1.24}$$

$$m_3 = \underbrace{\rho(\overrightarrow{r} \wedge \overrightarrow{v}) \cdot \overrightarrow{i_3}}_{due\ to\ the\ relative\ velocity} + \underbrace{\rho(\overrightarrow{r} \wedge (\overrightarrow{\Omega} \wedge \overrightarrow{r})) \cdot \overrightarrow{i_3}}_{due\ to\ the\ Earth's\ rotation} \tag{1.25}$$

The relative velocity of the air is described in spherical coordinates by :

$$\overrightarrow{v} = u\overrightarrow{e_\lambda} + v\overrightarrow{e_\phi} + w\overrightarrow{e_r} \tag{1.26}$$

Expressing the axial angular momentum in the spherical coordinate system defined in Fig. 1.6, it gives :

$$m_3 = \underbrace{\rho u r cos(\phi)}_{due\ to\ the\ relative\ velocity} + \underbrace{\rho \Omega r^2 cos(\phi)^2}_{due\ to\ the\ Earth's\ rotation} \tag{1.27}$$

$$m_3 = \rho(u + \Omega r cos(\phi)) r cos(\phi) \tag{1.28}$$

And therefore,

$$M_3 = \underbrace{\int_V \rho u r cos(\phi) dV}_{wind\ AAM} + \underbrace{\int_V \rho \Omega r^2 cos(\phi)^2 dV}_{mass\ AAM} \tag{1.29}$$

The part of the axial angular momentum (AAM) due to the relative velocity of the air is called wind AAM or relative AAM (M_r), and the part due to the rotation of the Earth is called mass AAM (referred to as M_o or M_Ω in the literature).

$$M_3 = \int_V \rho(u + \Omega r cos(\phi)) r cos(\phi) dV \tag{1.30}$$

In the following, we will only consider the axial angular momentum (AAM), and write $M = M_3$

1.3.2 Conservation law for Axial Angular Momentum (AAM)

The global axial angular momentum of the atmosphere is a particularly interesting quantity, due to its conservation law. Indeed, in the absence of orography (and pressure differences across mountains) and in the absence of friction, the global axial angular momentum of the atmosphere is conserved.

$$\frac{dM}{dt} = 0 \tag{1.31}$$

More generally, the AAM evolution is governed by [6]:

$$\frac{dM}{dt} = T_o + T_f \tag{1.32}$$

where

- T_o represents the global mountain torque (includes the torque due to pressure differences across the mountain ranges)
- T_f represents the friction torque. It accounts for the the exchange of angular momentum with the solid Earth surface due to surface friction.

1.4 Angular momentum conservation in General Circulation Models (GCM)

1.4.1 Conditions for a realistic atmospheric description

It is critical to have a realistic description of an atmosphere angular momentum in order to obtain realistic results with atmospheric GCM.
To do so, it is necessary to have realistic physical torques and parametrizations, and that the numerics does not lead to spurious sources / sinks of angular momentum. This latter point was the main focus of the internship : the goal was to check if the numerical sources / sinks of angular momentum in the simulations are negligible in comparison to the physical sources and sinks.
As mentioned in Section 1.1, the code is splitted into three different processes : the dynamics, the dissipation, and the physics. All of these processes are called one after another.
Formally, the hydrostatic primitive equations (HPE) conserve angular momentum, in the absence of surface torque and zonal mechanical forcing [21]:

$$\frac{dM}{dt} = 0 \tag{1.33}$$

As the AAM is conserved in the absence of orography and surface friction, the dynamics and dissipation processes should therefore not lead to changes in AAM and the changes in AAM should only come from the physics.
However, this is not the case with GCM, and both dynamics and dissipation processes do affect the AAM. The dynamical core DYNAMICO does not conserve AAM to machine precision. These numerical torques due to the dynamics and the dissipation are spurious sources or sinks of AAM, as they do not represent any physical process. One has to make sure that these spurious sources / sinks of AAM are much smaller than the physical torques, coming from the physics.
One can write :

$$\frac{dM}{dt} = \left(\frac{dM}{dt}\right)_p + \left(\frac{dM}{dt}\right)_\epsilon \tag{1.34}$$

with $\left(\frac{dM}{dt}\right)_p$ being the parametrized physical torques (due to pressure differences across mountains and to surface friction) and $\left(\frac{dM}{dt}\right)_\epsilon$ the (spurious) torques due to the numerics (dynamics and dissipation). One would like to have :

$$\left(\frac{dM}{dt}\right)_\epsilon << \left(\frac{dM}{dt}\right)_p$$

and therefore :

$$\frac{dM}{dt} \approx \left(\frac{dM}{dt}\right)_p \tag{1.35}$$

1.4.2 Calculation of AAM in the code

The globally integrated axial angular momentum is computed by adding elementary angular momentum of each cell of the mesh.

$$M = M_r + M_o = \underbrace{\int_V \rho u r cos(\phi) dV}_{wind\ AAM} + \underbrace{\int_V \rho \Omega r^2 cos(\phi)^2 dV}_{mass\ AAM} \tag{1.36}$$

$$M_r = \int_V \rho u r cos(\phi) dV = \int_V u r cos(\phi) \rho dV = \int_V u r cos(\phi) dm \approx \sum_i u_i r_i cos(\phi_i) \cdot m_i$$

With i being an index going through all the cells of the mesh, u_i the associated cell velocity, m_i the associated cell mass, and r_i, ϕ_i the associated cell position (radius and latitude).
Similarly,

$$M_o = \int_V \rho \Omega r^2 cos^2(\phi) dV = \int_V \Omega r^2 cos^2(\phi) dm \approx \sum_i r_i cos(\phi_i) \cdot m_i \cdot r_i \Omega cos(\phi_i)$$

1.4.3 Calculation of the different torques in the code

The wind, mass and total AAM are calculated before and after each call of the dynamics, the dissipation and the physics. One can therefore know the AAM variation ocuring during the call to the dynamics, the dissipation, and the physics, as schematized in Fig. 1.12.

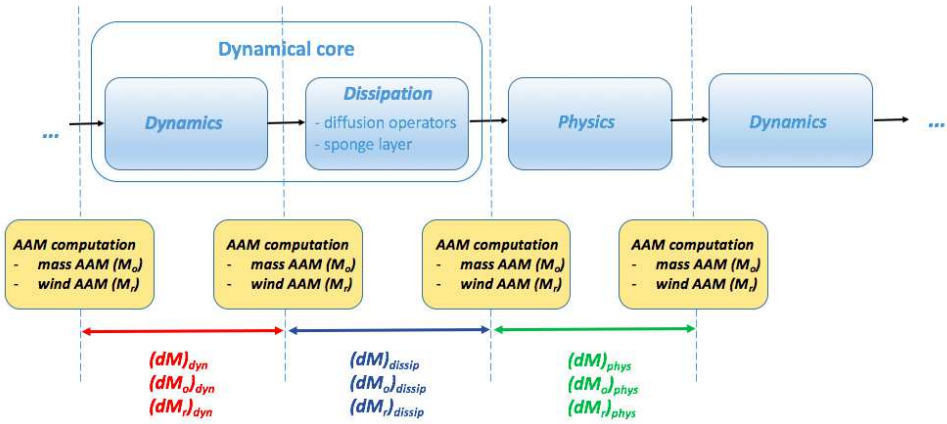

FIGURE 1.12 – Schematic representation of the computation of the AAM variations.

As it would take too much storage space to store the AAM variations every time a process is called, the approximation is made that :

$$\frac{dAAM}{dt} = \frac{\delta AAM}{\delta t} \tag{1.37}$$

with δAAM beeing the AAM variation during time δt. δt is often choosen as a multiple of the simulation timestep Δt. For example, in the idealized Earth's simulation carried out during this internship, the AAM variations were written every day, and 72 times per Venus day for the idealized Venus simulation.
One should not take a too small δt due to storage limits. One should also not take a too large δt, otherwise the AAM variations $\frac{dAAM}{dt}$ would be too smoothed.
As an output of the simulation, one can have the mass and wind AAM at every checked timestep (timestep at which the AAM informations are written). One can obtain the variations of the mass AAM due to the physics, the dynamics and the dissipation, as well as the variations of the

wind AAM due to the physics, the dynamics and the dissipation.
The physics and the dissipation do not affect the mass AAM, as these processes only affect the wind field. Therefore $(\frac{dM_o}{dt})_p = 0$ and $(\frac{dM_o}{dt})_{dissip} = 0$. The dynamics does affect the mass AAM. Mass AAM variation due to the dynamics are $(\frac{dM}{dt})_{mass\ dyn} = (\frac{dM_o}{dt})_{dyn}$, also referred to as the **"mass dyn"** torques in the following.
Both the physics, the dynamics and the dissipation do affect the wind (relative) AAM. The wind AAM changes due to the dynamics, $(\frac{dM}{dt})_{vel\ dyn} = (\frac{dM_r}{dt})_{dyn}$, are also referred to as the **"vel dyn"** torque in the following. The AAM changes due to the dissipation and due to the physical parametrizations (physics) are called **dissipation torque** $(\frac{dM}{dt})_{dissip}$ and **torques from the physical parametrization** $(\frac{dM}{dt})_p$
The total AAM changes are :

$$\frac{dM}{dt} = (\frac{dM}{dt})_p + (\frac{dM}{dt})_{dissip} + (\frac{dM}{dt})_{dyn}$$

The changes in total AAM due to the dynamics, called the **dynamical torques**, or torques due to the dynamics are :

$$(\frac{dM}{dt})_{dyn} = (\frac{dM}{dt})_{vel\ dyn} + (\frac{dM}{dt})_{mass\ dyn}$$

The total spurious changes in AAM (called **numerical torques**) are the sum of the dynamical and dissipation torques :

$$(\frac{dM}{dt})_{\epsilon} = (\frac{dM}{dt})_{dyn} + (\frac{dM}{dt})_{dissip}$$

The AAM variations due to the dissipation torques are composed of the AAM variations due to the **explicit diffusion operators torques** (D) and to the **sponge layer torques** (S).

$$(\frac{dM}{dt})_{dissip} = D + S$$

The contribution from the sponge layer is given by :

$$S = \int_V \rho a cos(\phi)(\frac{du}{dt})_{Sp} dV \tag{1.38}$$

with $(\frac{du}{dt})_{Sp}$ the wind variations due to the sponge layer :

$$(\frac{du}{dt})_{Sp} = \begin{cases} -k_{Sp}(p) \cdot u \quad for\ the\ 3\ or\ 4\ top\ levels \\ 0\ elsewhere\ (k_{Sp}(p) = 0) \end{cases} \tag{1.39}$$

However, it is not possible to distinguish the two contributions D and S with the current setup, as the AAM is computed only before and after the call to the dissipation, and not after each of theses processes separately.
In the simulations carried out during the thesis, as will be detailed in Section 2.2 for the Earth case and Section 3.2 for the case of Venus, the only physical parametrization in the test cases come from the friction at the surface, and there is no orography. Therefore the torque from the physical parametrization can be expressed as :

$$(\frac{dM}{dt})_p = \int_V \rho a cos(\phi)(\frac{du}{dt})_s\ dV$$

with a being the planetary radius, ϕ the latitude, $(\frac{du}{dt})_s$ the surface wind variations and V the atmosphere volume.

In the following of the thesis, the AAM changes due to either the physical parametrization ($(\frac{dM}{dt})_p$), the dynamics ($(\frac{dM}{dt})_p$), the dissipation ($(\frac{dM}{dt})_{dissip}$), the numerics ($(\frac{dM}{dt})_{\epsilon} = (\frac{dM}{dt})_{dyn} + (\frac{dM}{dt})_{dissip}$) will also be referred to as parametrized torques (τ_p), dynamical torques (τ_{dyn}), dissipation torques (τ_{dissip}), numerical torques (τ_ϵ).

2

The Held Suarez test case for the Earth's atmosphere

2.1 The Earth's general atmospheric simulation

In this section, we will describe some of the main features of the Earth's atmosphere.

2.1.1 Thermal structure

The net radiative budget of the Earth's atmosphere over the year shows a net surplus of incoming radiations in the tropics and a net deficit in the poles, as can be seen in Fig. 2.1. This results in warmer temperatures at the equator, and colder near the poles. This horizontal temperature gradient is a major driver of the atmospheric dynamics. Indeed, as local energy balance must be satisfied, this implies that energy is transported from low latitudes (equator) to higher latitudes (the pole), to maintain this equilibrium.

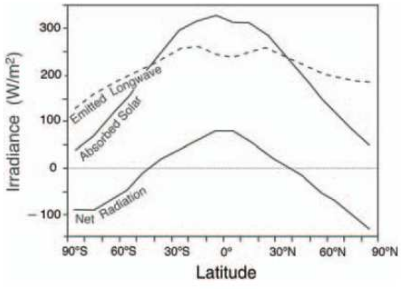

FIGURE 2.1 – Annual mean absorbed solar radiation ,emitted long-wave radiation, and net radiation, the sum of the two. Picture and legend from [13].

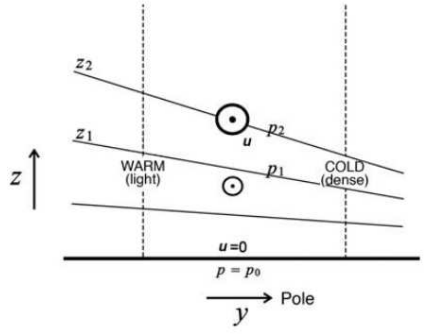

FIGURE 2.2 – Warm columns of air expand, cold columns contract, leading to a tilt of pressure surfaces, a tilt which typically increases with height in the troposphere. Picture and legend from [13].

Through balance, this horizontal temperature gradient induces an horizontal pressure gradient, as schematized in figure Fig. 2.2 : warm air expands, whereas cold air contracts, which tilts the pressure surfaces and creates an horizontal pressure gradient. For more details, see Section 5.2.

2.1.2 Wind distribution

A short help for plot reading is provided in Section 5.1. The zonal wind u (east-west component) averaged over the year and over longitude (zonally) is represented in Fig. 2.3. The winds are

predominantly eastward ($u > 0$) in green, apart from around the equator (beige color). There are two strong subtropical jets, located around 30 degrees latitude in each hemisphere, with wind speed reaching $30m \cdot s^{-1}$.

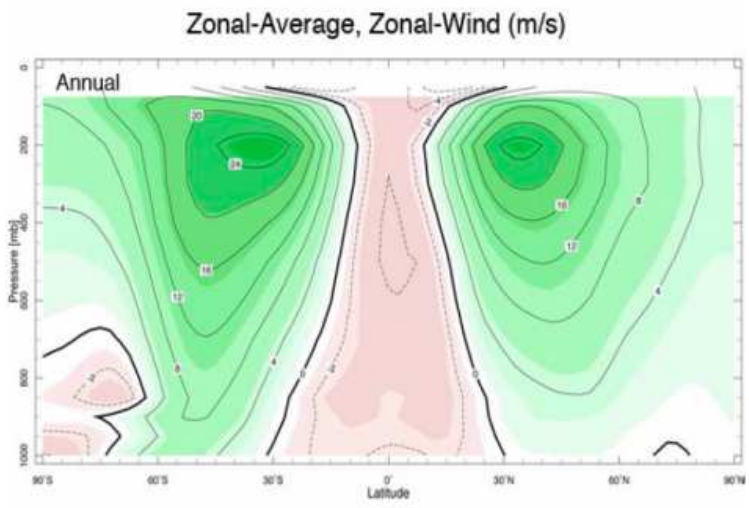

FIGURE 2.3 – zonal wind of the Earth's atmosphere, in annual mean. Picture from [13]. The x-axis represents the latitude, and the y- axis represents the pressure. The bottom corresponds to the Earth surface and the top to the atmosphere's top.

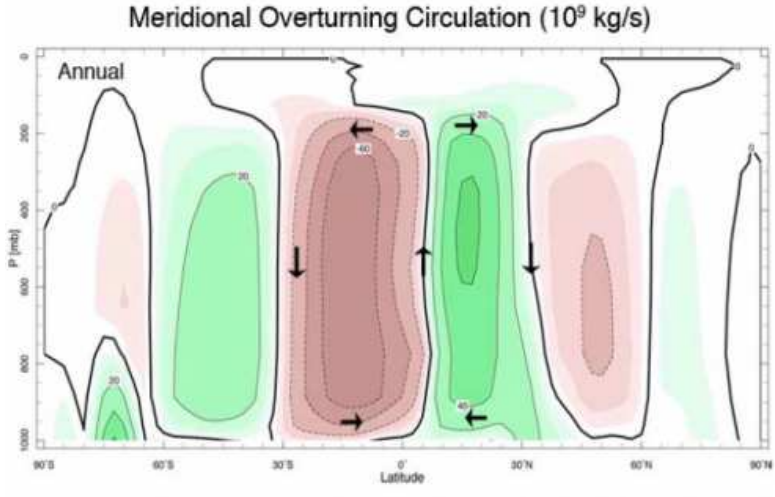

FIGURE 2.4 – meridional overturning circulation of the Earth's atmosphere in annual mean. Picture from [13]. The x-axis represents the latitude, and the y- axis represents the pressure. The bottom corresponds to the Earth surface and the top to the atmosphere's top.

The meridional overturning circulation (ie the zonal-mean circulation of the atmosphere in the meridional plane) in annual mean is represented in Fig. 2.4. The atmospheric circulation consists of different cells. The one near the equator is called the Hadley cell : there is a rising motion next to the equator and a descending motion around 30 degrees of latitude. The cells located in the middle latitudes are called Ferrel cells : they are weaker reverse cells. They are associated with midlatitude eddies that result from the nonlinear evolution of the baroclinic instability. Strictly speaking, they do not correspond to a steady and zonally uniform cell. Indeed, the

zonally averaged plots give an unrealistic view of the atmosphere, which is strongly varying with time and longitudes.

2.2 The Held Suarez test case

2.2.1 Description of the test case

The Held Suarez configuration [8] is an idealized Earth configuration which serves the purpose of evaluating the dynamical core of atmospheric GCM independently of the physical parametrizations.
In this configuration, the detailed radiative, turbulence and moist convective parametrizations are replaced by simple forcing and damping prescriptions :

- Temperatures are relaxed toward a prescribed, zonally symmetric "radiative equilibrium" $T_{eq}(P, \phi)$. This radiative equilibrium depends on latitude and pressure (and therefore, height).
$$\frac{\partial T}{\partial t} = ... - k_T(T - T_{eq}(\phi, p))$$
- The low-level winds are damped using a Rayleigh damping, in order to represent boundary-layer friction.
$$\frac{\partial \mathbf{u}}{\partial t} = ... - k\mathbf{u}$$
with k (damping coefficient, in s^{-1}) equal to zero outside the first vertical levels of the mesh.

In this configuration, there is no topography.
This simple forcing and dissipation result in a quite realistic zonal mean circulation, shown in Fig. 2.5. Indeed, the statistical mean state is comparable to the one of the Earth's atmosphere (Fig. 2.3) in terms of temperature profile and zonal jet-streams [8]. The circulation obtained with the Held Suarez setting is highly idealized and symmetric around the equator, as the physics was simplified and there is no topography, but it is a classical configuration used to test Earth GCM.

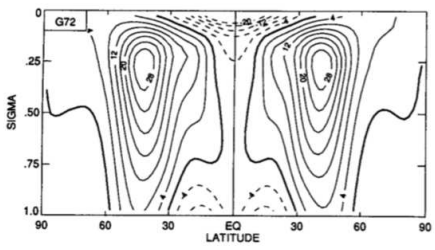

FIGURE 2.5 – Picture from [8]: zonal mean zonal wind obtained with the Held Suarez settings.

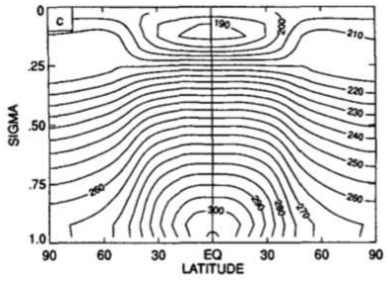

FIGURE 2.6 – Picture from [8]: temperature obtained with the Held Suarez settings.

In this setup, the only physical source/ sink of AAM is due to the Rayleigh damping, as there are no large mountain torques and no large subgrid scale torques. Therefore, it is an appropriate setup to test the AAM conservation properties of an atmospheric GCM. Indeed, in realistic simulations that include orography, the large mountain torque may mask the lack of AAM conservation, as the spurious sources / sinks of AAM will always remain small compared to the physical mountain torque. Checking the AAM budget in Held Suarez configuration is therefore a critical test to perform. If the AAM budget is satisfying in the Held Suarez test case, it should be satisfying in a real Earth configuration.
Held Suarez simulations are usually run for 1200 days.

2.2.2 Limitations due to the test case

With this setup it is not possible to exactly attribute how many percent of the computed AAM come from physical sources, as both dynamical and physical terms feedback on one another. Indeed, the only parametrized sources and sinks of AAM in this setup are the friction torques at the surface, $\tau_p = \int_V \rho a cos(\phi)(\frac{du}{dt})_s \, dV$. τ_p depends on the surface winds (winds in the first vertical layers), which itself depends on the general circulation. If the circulation is not solved accurately (because of numerical errors), this leads to inaccurate surface winds, which in turn lead to inaccurate physical parametrizations. Consequently, the AAM variations are also different, and the general circulation obtained as well. Furthermore, the dynamical errors depend on the circulation, as will be seen in Section 3.5 : different kind of circulation can lead to different numerical errors. This coupling between the numerical errors and the physical parametrization is schematized in Fig. 2.7.

With the setup used and the indicators of the AAM budget quality developed during this thesis, it is possible to compare the share of the AAM content and fluctuations due to either the physical parametrizations or the numerical errors, and to know if the AAM content and fluctuations are mainly driven by numerical errors or the parametrized AAM sources. However, it is not possible to know what the AAM content and fluctuations would have been in a simulation without numerical errors. The informations obtained on the AAM budget quality cannot be directly applied to determine if the circulation obtained is closer to what it would be in the case of a simulation without numerical errors.

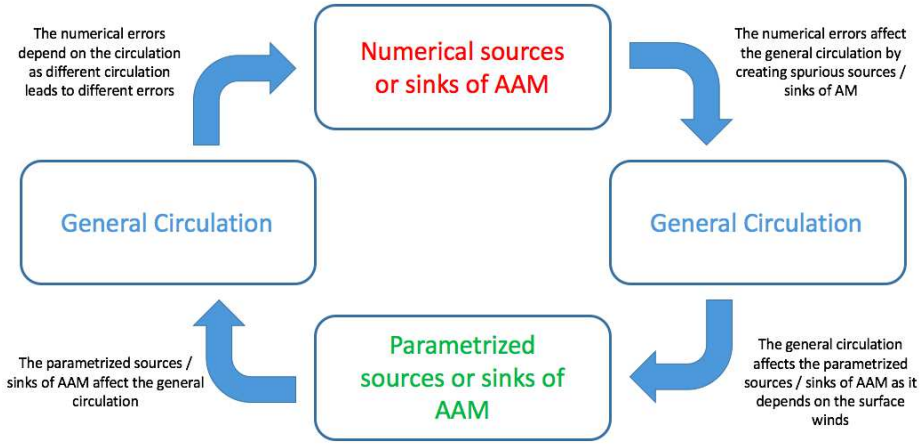

FIGURE 2.7 – schematic explanation of the coupling between the spurious AAM sources / sinks coming from the dynamics and the parametrized physical sources. With this configuration it is impossible to fully decouple the spurious numerical torques and the parametrizations, and it is therefore impossible to know the exact physical or non physical share of AAM.

2.3 Reference simulation

The reference simulation (called "baseline simulation") has the following parameters :

- resolution : nbp = 41, llm = 39
- there is no sponge layer at the model top
- The explicit diffusion operator are of second order, with a time constant equal to 10 000 s, which is typical of Earth simulations.

2.3.1 General circulation

Zonal and meridional wind

The general circulation obtained in our baseline simulation is really close to the circulation obtained by Held and Suarez [8]. Fig. 2.5 shows the zonal mean zonal wind obtained in the Held Suarez paper [8] and Fig. 2.8 show the zonal mean zonal wind obtained with the baseline simulation run on DYNAMICO.

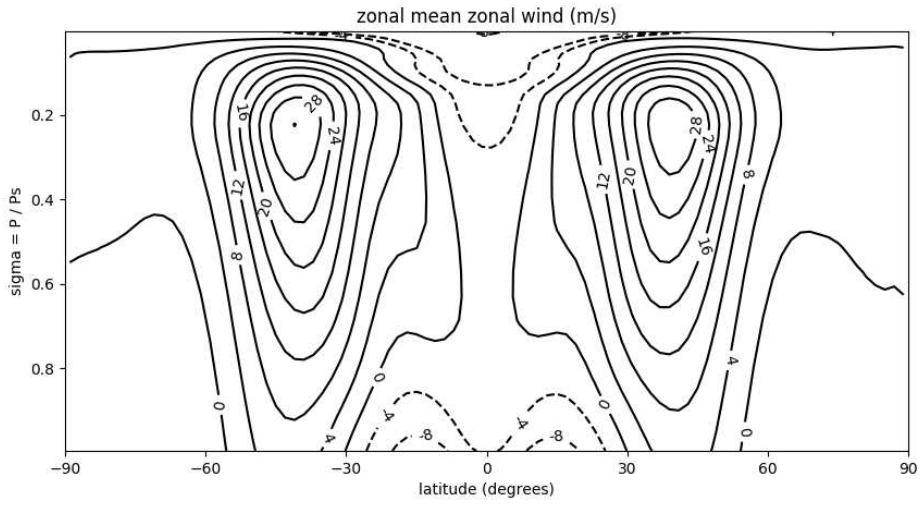

FIGURE 2.8 – zonal mean zonal wind : U (m/s), as a function of $\sigma = p/p_s$ with p the pressure and p_s the surface pressure

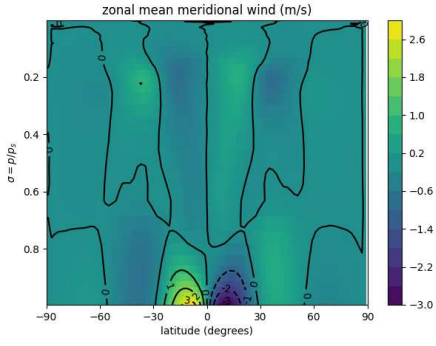

FIGURE 2.9 – meridional velocity

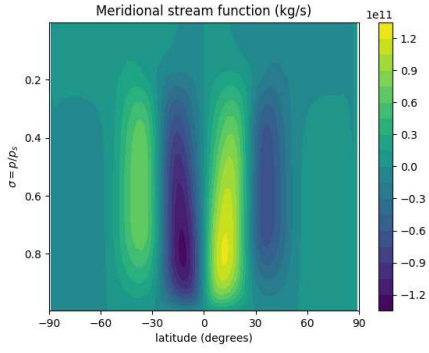

FIGURE 2.10 – streamlines

The meridional velocity v (Fig. 2.9) is negative in the low latitudes of the Northern hemisphere, close to the surface. The meridional velocity then becomes positive at higher altitude. This corresponds to a Hadley cell, with rising motions near the equator. This can also be seen with the streamlines in Fig. 2.10 : there are two dominant Hadley cells near the equator, and reversed cells at middle latitudes. For more details on the streamlines see Section 5.3.

Temperature

The temperature, plotted in Fig. 2.11 is similar to the one obtained by Held Suarez, shown in Fig. 2.6.

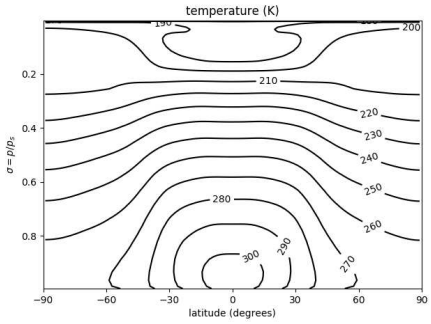

FIGURE 2.11 – temperature

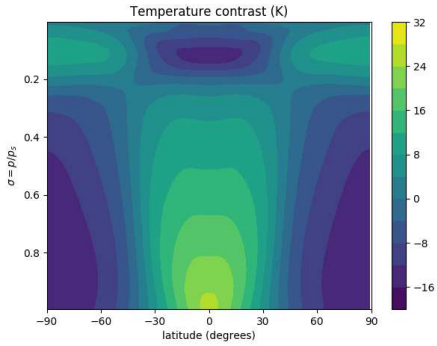

FIGURE 2.12 – temperature contrast

The temperature contrast represents the difference to the temperature $T(p)$, averaged zonally, over time and over latitudes, at a certain pressure. The temperature contrast is negative at the poles at higher pressure (lower altitudes), and positive at the equator : the poles are colder than the equatorial region. However, this temperature contrast is reversed for pressures lower than (altitudes higher than) $P \approx 2 \cdot 10^4$ Pa, i.e. $\sigma = p/p_s < 0.2$ with p_s the surface pressure.
The thermal wind relation for geostrophic balance seems to hold quite well qualitatively : a decrease (increase) of temperature toward the poles corresponds to an increase (decrease) of the zonal wind velocity with altitude. For more details on the thermal wind equation, see Section 5.2.

2.3.2 Angular momentum budget

Total, wind, mass and normalized AAM

In the Held Suarez setup, the AAM is dominated by the mass AAM, as visible in Fig. 2.13 : the mass AAM (cyan curve) is much larger than the wind AAM (brown curve) : the total AAM value (orange curve) is close to the mass AAM value.

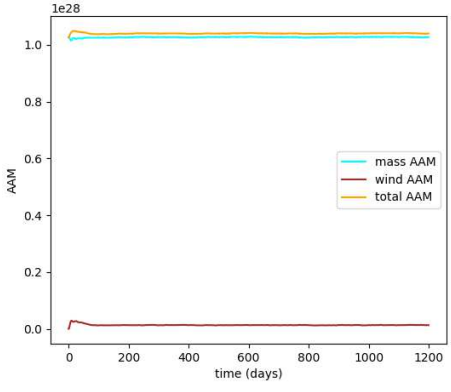

FIGURE 2.13 – Evolution of the AAM over time in the baseline simulation

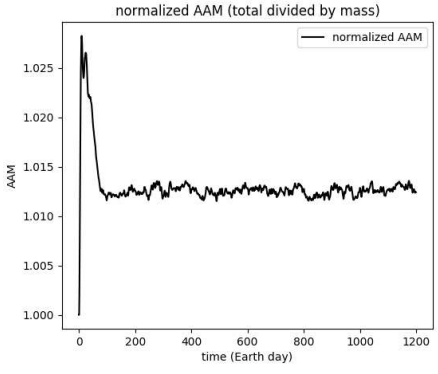

FIGURE 2.14 – Evolution of the normalized AAM (total divided by mass) in the baseline simulation

A statistically steady state is reached rapidly, around approximately 100 days. The determination of the steady state is based on the normalized AAM (total AAM divided by the mass AAM), shown in Fig. 2.14. From 100 days onward, the normalized AAM is varying by less than 0.1 % around its mean value.
During the steady state, the mass AAM oscillates around $1.027 \cdot 10^{28}\ kg \cdot m^2 \cdot s^{-1}$, with deviations

of order $10^{25}\ kg \cdot m^2 \cdot s^{-1}$.
The wind AAM is equal to $1.292 \cdot 10^{26} kg \cdot m^2 \cdot s^{-1}$, with deviations of order $10^{25}\ kg \cdot m^2 \cdot s^{-1}$. The total AAM oscillates around $1.040 \cdot 10^{28} kg \cdot m^2 \cdot s^{-1}$, with deviations of order $10^{25}\ kg \cdot m^2 \cdot s^{-1}$. These values are close to real Earth AAM, concerning both their mean and deviations [6]. Real Earth wind AAM oscillates around $1.5 \cdot 10^{26} kg \cdot m^2 \cdot s^{-1}$, with standard deviation $2 \cdot 10^{25}\ kg \cdot m^2 \cdot s^{-1}$, and the mass AAM oscillates around $1 \cdot 10^{28} kg \cdot m^2 \cdot s^{-1}$, with standard deviation $6 \cdot 10^{24}\ kg \cdot m^2 \cdot s^{-1}$.

Torques

The torques affecting the AAM over the simulation are represented in Figs. 2.15, 2.16, 2.17. Fig. 2.15 represents the torques over the whole simulation : the torques due to the dynamics (red curve), the torques due to the physical parametrizations (green curve) the torques due to the dissipation (blue curve) and the total torques, sum of the 3 previous torques (purple). There is a short spin-up with relatively high value of the total torques (compared to the rest of the simulation) in the 100 first days. The transient part of the simulation is rapid, and a steady state is reached after approximately 100 days, with $\left\langle \frac{dM}{dt} \right\rangle \approx 0$, with $\langle\rangle$ representing the time mean. Fig. 2.16 is a zoom of Fig. 2.15 on the steady state period (days 600-1200 for the figure).

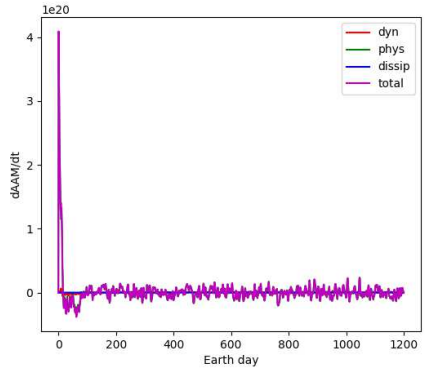

FIGURE 2.15 – Evolution of the AAM torques over the whole simulation

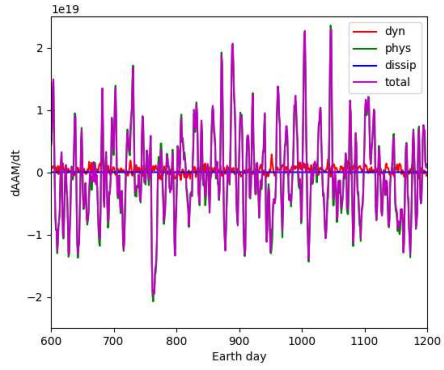

FIGURE 2.16 – Evolution of the AAM torques over the last 600 days of the simulation

One can see on Fig. 2.16 that the total torques and torques due to the physical parametrization (green and purple curves) overlap significantly. The dissipation torques (blue curve) are undistinguishable from the zero line. The torques due to the dynamics (red curve) are much smaller than the parametrized and total torques.
Fig. 2.17 represents the different torques as in Fig. 2.16 but splitted in the different contributions : the relative contributions to the changes in AAM due to either, the dynamics (first row), i.e. the dynamical torques $\left(\frac{dM}{dt}\right)_{dyn} = \tau_{dyn}$, the dissipation $\left(\frac{dM}{dt}\right)_{dissip} = \tau_{dissip}$ (second row) , and the physical parametrizations $\left(\frac{dM}{dt}\right)_{p} = \tau_p$ (third row) . These torques are divided into the contribution to the total AAM changes (first column), wind AAM changes (second column), and mass AAM changes (third column). For example, the mass AAM changes due to the dynamics are located in the third column of the first row.
The torques coming from the dissipation (third row) are of order $10^{15}\ kg \cdot m^2 \cdot s^{-2}$. This is four order of magnitude smaller than the parametrized torques : $\left(\frac{dM}{dt}\right)_{dissip} << \left(\frac{dM}{dt}\right)_{p}$.
In this simulation, as no sponge layer is used at the model top, the contribution from the dissipation only comes from the explicit diffusion operators : their impact is negligible.
The dynamical sources / sinks of AAM are one order of magnitude smaller than the parametrized sources / sinks. It can be seen from the first row of Fig. 2.17, that the amplitude of the variations of mass and wind AAM due to the dynamics are or order $10^{19}\ kg \cdot m^2 \cdot s^{-2}$: $\left(\frac{dM}{dt}\right)_{vel\ dyn} \approx -\left(\frac{dM}{dt}\right)_{mass\ dyn}$. The sum of these two contributions is of order $10^{18}\ kg \cdot m^2 \cdot s^{-2}$: $\left(\frac{dM}{dt}\right)_{dyn} << \left(\frac{dM}{dt}\right)_{p}$.

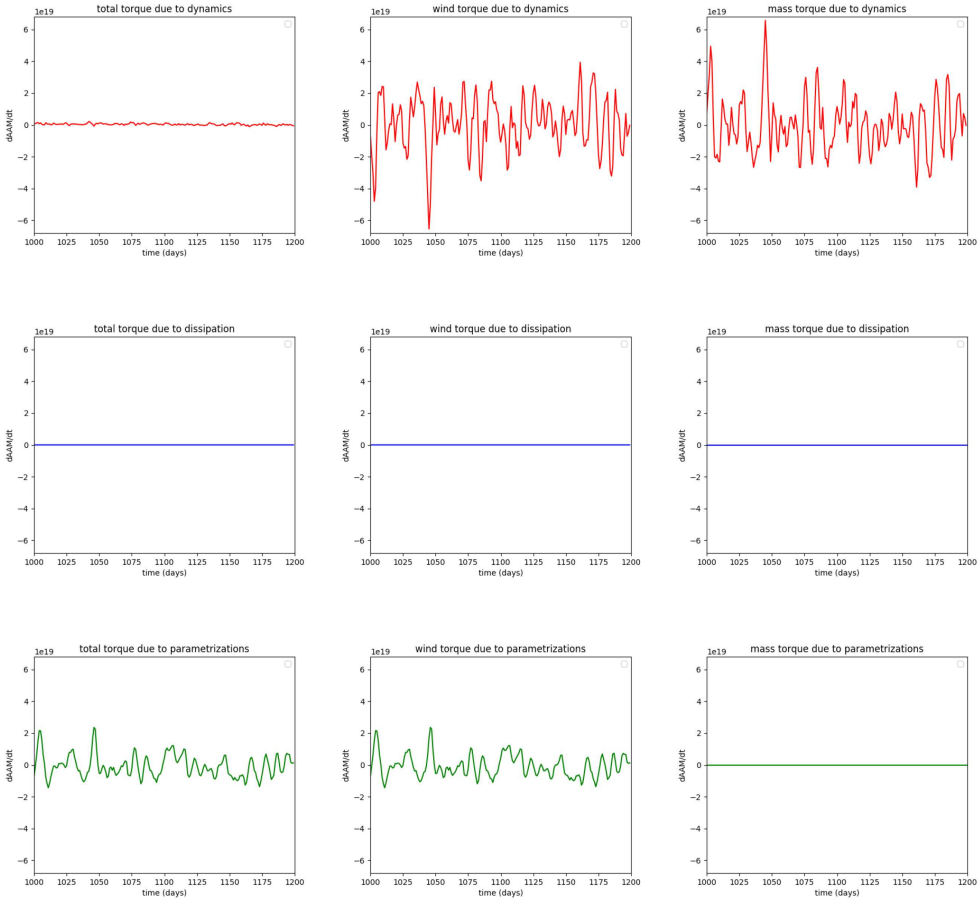

FIGURE 2.17 – First row : torques due fo the dynamics (dyn). Second row : time torques of AAM due fo the dissipation (dissip). Third row : physical parametrizations torques (phys).

Indicators of the AAM budget quality

As stated in Section 2.2, it is not possible to exactly attribute how many percent of the computed AAM come from physical sources, as both dynamical and parametrized terms feedback on one another with the Held Suarez setup.
However, one can define two important criteria in order to have a satisfying AAM budget :

- the AAM value reached at the end of the transient should come mostly from the physical parametrizations.
- during the steady state, AAM fluctuations should be dominated by the physical parametrizations.

To quantify the share of AAM due to the physical parametrization injected during the transient part (first criterion), we used the indicator $\frac{\int_{t_0}^{t_{ss}} \tau_p \ dt'}{\int_{t_0}^{t_{ss}} \tau_{tot} \ dt'}$. t_{ss} represents the time at which the steady state is reached. This indicator represents the integral of the parametrized torques over the integral of the total torques during the transient. To have a satisfying AAM budget, this indicator should be as close as possible to one, meaning that all of the angular momentum injected into the atmosphere during the transient part comes from the physical parametrizations. On the contrary, $\frac{\int_{t_0}^{t_{ss}} \tau_\epsilon \ dt'}{\int_{t_0}^{t_{ss}} \tau_{tot} \ dt'}$, the ratio of the integral of the numerical torques over the integral of the total torques during the transient should be as close as possible to zero.
To quantify the importance of the fluctuations due to the numerical errors or to the dynamics during the steady state (second criterion), we used the indicators $\frac{\sigma_\epsilon}{\sigma_{tot}}$ and $\frac{\sigma_p}{\sigma_{tot}}$ estimated over the steady-state period, with σ_ϵ, σ_p, σ_{tot} being the standard deviations of the numerical, parametrized and total torques. To have a satisfying AAM budget $\frac{\sigma_\epsilon}{\sigma_{tot}}$ should be as close as possible to zero and $\frac{\sigma_p}{\sigma_{tot}}$ as close as possible to one, meaning that all the AAM fluctuations during the steady state come from the parametrized torques.
As explained in [24], the square of the Pearson correlation coefficient (called determination coefficient, r^2 in the following) of two variables x and y specifies the proportion of the variability of one variable which is linearly explained (described) by the other. The Pearson correlation coefficient is bounded by -1 and 1. In the case where it is equal to 1, there is a perfect linear association between the two variables x and y. In the case where it is equal to -1, there is a perfect negative association. However, the correlation and determination coefficient do not provide any explanation on the relationship between the variables x and y, in a physical or causative sense. It could be that x physically causes y or inversely. If there were no numerical errors, the total torques and the parametrized torques would have a determination coefficient of 1, and the numerical torques and the total torques would have a determination coefficient of 0. To have a satisfying AAM budget, $r^2(\tau_\epsilon, \tau_{tot})$ should be as close as possible to zero and $r^2(\tau_p, \tau_{tot})$ should be as close as possible to 1.
These indicators were also calculated by considering only the dynamics (second column of Table 2.1, α = dyn), or only the dissipation (third column of Table 2.1, α = dissip), or the dynamics and the dissipation (fourth column of Table 2.1, $\alpha = \epsilon = dissip + dyn$), in order to study the relative importance of these two processes (dynamics and dissipation) in the total numerical errors.
As visible in Table 2.1 the indicators obtained for the baseline simulation when only the dynamics is considered, or the dissipation and dynamics are both considered are equal, indicating again that the dissipation has a negligible role.
A sensitivity study to the definition of the steady-state was performed. These indicators do not vary (at least up to the digit considered here) when the start of the steady state is taken at 80, 100 or 200 days.
The indicators $\frac{\int_{t_0}^{t_{ss}} \tau_\epsilon \ dt'}{\int_{t_0}^{t_{ss}} \tau_{tot} \ dt'}$ and $\frac{\int_{t_0}^{t_{ss}} \tau_p \ dt'}{\int_{t_0}^{t_{ss}} \tau_{tot} \ dt'}$ are equal to -0.11 and 1.11, showing that most of the AAM injected into the atmosphere during the transient part comes from the parametrized torques.
During the steady state, the mean parametrized torque applied is $\overline{\tau_p} = -1.88 \cdot 10^{17} \ kg \cdot m^2 \cdot s^{-2}$ and the mean numerical torque is $\overline{\tau_\epsilon} = 2.59 \cdot 10^{17} \ kg \cdot m^2 \cdot s^{-2}$. However, the variability (calculated through the standard deviation) is much stronger for the parametrized torques : it is 13 times

	$\alpha =$ dyn	$\alpha = dissip$	$\alpha = \epsilon = dissip + dyn$
$\frac{\int_{t_0}^{t_{ss}} \tau_\alpha \ dt'}{\int_{t_0}^{t_{ss}} \tau_{tot} \ dt'}$	-0.11	-1.4e-5	-0.11
$\frac{\int_{t_0}^{t_{ss}} \tau_p \ dt'}{\int_{t_0}^{t_{ss}} \tau_{tot} \ dt'}$	1.11	-	-
$\frac{\sigma_\alpha}{\sigma_{tot}} \ (SS)$	0.08	2.4e-5	0.08
$\frac{\sigma_p}{\sigma_{tot}} \ (SS)$	1.01	-	-
$r^2(\tau_\epsilon, \tau_{tot})$	0.09	7e-4	0.09
$r^2(\tau_p, \tau_{tot})$	0.998	-	-

TABLE 2.1 – Different indicators of the quality of the AAM budget for the baseline simulation.

higher than the variability of the numerical torques from the dynamical core, with a standard deviation of $6.87 \cdot 10^{18} \ kg \cdot m^2 \cdot s^{-2}$ for the parametrized torques and $5.46 \cdot 10^{17} \ kg \cdot m^2 \cdot s^{-2}$ for the numerical ones. As $\frac{\sigma_\epsilon}{\sigma_{tot}} = 0.08$ and $\frac{\sigma_p}{\sigma_{tot}} = 1.01$ over the steady-state, most of the total AAM fluctuations come from the parametrized torques.

The parametrized torques and the AAM variations have a determination coefficient of 0.993 during the steady state, 0.9997 during the transient part of the simulation and 0.999 over the whole simulation. The parametrized and total torques are strongly correlated. Inversely, the numerical torques and the AAM changes have a determination coefficient of 0.423 during the transient, 0.002 during the steady state and 0.09 over the whole simulation : the numerical and total torques are weakly correlated.

With all the previous indicators, we can conclude that in the baseline simulation most of AAM content and fluctuations result from the physical parametrization.

Statistical analysis of the torques

As can be graphically seen in Fig. 2.18, and from the previous analysis (the mean numerical torque estimated over the simulation length is $\overline{\tau_\epsilon} = 2.59 \cdot 10^{17} \ kg \cdot m^2 \cdot s^{-2}$), the numerical torques (mainly coming from the dynamical torques, as the dissipation is negligible in this simulation) seem to have a small, but positive and non zero long term average.

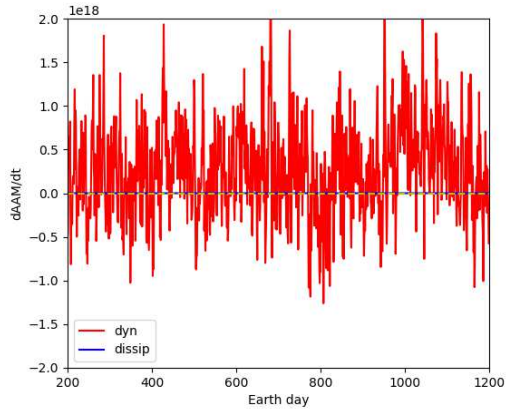

FIGURE 2.18 – Torques due to the dynamics (red) and to the dissipation (blue). The dashed yellow line represents the axis y = 0.

However, as the standard deviation is high, one needs to know if the obtained positive mean of the numerical torques on the simulation is significative. To do so, we used statistical methods. If we suppose that the torques are following a distribution of expected value m and finite standard deviation s, it is possible, based on the empirical mean μ and empirical standard deviation σ calculated on a sample, to obtain a confidence interval for the expected value m.
In the following, we will call μ the empirical mean, the mean obtained on the simulation (sample), and $\langle\rangle$, the expected value. The two different methods used are :

- Approximation by central limit theorem (CLT)
- Bootstrap method

More details are given in Section 5.4.1. These methods allow to obtain a 95 % confidence interval of the expected value, based on the empirical mean and standard deviation of the sample. These two methods gave similar results. For the approximation by CLT the confidence interval for the expected value is given directly by :

$$I_c = [\mu - q\frac{\sigma}{\sqrt{n}}, \mu + q\frac{\sigma}{\sqrt{n}}] \tag{2.1}$$

with μ and σ the sample mean and standard deviation, n the size of the sample, and q the 95% quantile, q = 1.96. The bootstrap method is based on random draws and was implemented with Python.
In the baseline simulation, the empirical means (μ) and standard deviations (σ) of the sample (during the steady state) are :

- $\mu_{tot} = -7.06 \cdot 10^{16}$, $\sigma_{tot} = 6.83 \cdot 10^{18}$ for the total torques.
- $\mu_{dyn} = 2.59 \cdot 10^{17}$, $\sigma_{dyn} = 5.46 \cdot 10^{18}$ for the torques from the dynamics.
- $\mu_p = -1.88 \cdot 10^{17}$, $\sigma_p = 6.87 \cdot 10^{18}$ for the torques from the parametrizations.
- $\mu_{dissip} = -3.96 \cdot 10^{13}$, $\sigma_{dissip} = 1.64 \cdot 10^{14}$ for the torques from the dissipation.

The corresponding confidence interval (I_c) obtained for the expected value of the total torques ($\langle\tau_{tot}\rangle$), dynamical torques ($\langle\tau_{dyn}\rangle$), parametrized torques ($\langle\tau_p\rangle$), dissipation torques ($\langle\tau_{dissip}\rangle$) with the CLT and bootstrap (BTS) methods are :

$$\langle\tau_{tot}\rangle \in \begin{cases} [-3.6, 5.02] \cdot 10^{17} \ (CLT) \\ [-3.41, 5.01] \cdot 10^{17} \ (BTS) \end{cases}, 0 \in I_c$$

$$\langle\tau_{dyn}\rangle \in \begin{cases} [2.24, 2.93] \cdot 10^{17} \ (CLT) \\ [2.24, 2.93] \cdot 10^{17} \ (BTS) \end{cases}, I_c > 0$$

$$\langle\tau_p\rangle \in \begin{cases} [-6.22, 2.46] \cdot 10^{17} \ (CLT) \\ [-6.04, 2.46] \cdot 10^{17} \ (BTS) \end{cases}, 0 \in I_c$$

$$\langle\tau_{dissip}\rangle \in \begin{cases} [-5.0, 2.9] \cdot 10^{13} \ (CLT) \\ [-4.98, 2.95] \cdot 10^{13} \ (BTS) \end{cases}, 0 \in I_c$$

The entire confidence interval for the expected value of the dynamical torques is over zero : $I_c(\langle\tau_{dyn}\rangle) > 0$. This allows to conclude that the dynamical torques have a positive mean. However, with this 1200 days simulation, one cannot conclude on the sign of $\langle\tau_p\rangle$ and $\langle\tau_{tot}\rangle$, as the confidence interval has positive and negative values : zero is in the confidence interval, $0 \in I_c(\langle\tau_p\rangle)$ and $0 \in I_c(\langle\tau_{tot}\rangle)$.
Theoretically one would like to have :

$$\left\langle \frac{dM}{dt} \right\rangle = \langle\tau_{tot}\rangle = \langle\tau_p\rangle = 0$$

But in practice, one has :

$$\left\langle \frac{dM}{dt} \right\rangle = \langle\tau_{tot}\rangle = \langle\tau_p\rangle + \langle\tau_\epsilon\rangle$$

In our baseline simulation, the numerical torques almost entirely come from the dynamics ($\tau_\epsilon \approx \tau_{dyn}$), and

$$\langle \tau_{dyn} \rangle > 0, \ \langle \tau_\epsilon \rangle > 0$$

To know if $\langle \tau_{tot} \rangle > 0$ (or $\langle \tau_{tot} \rangle < 0$) is particularly important. It would mean that the atmosphere is continuously gaining (or loosing) angular momentum.
We can define the time t_a, at which the total angular momentum would be affected by 10 % by the non-zero total torques, i.e. the time at which the AAM would reach 110 % or 90 % of its theoretical steady-state value.

$$t_a = 0.1 \frac{M_{tot}}{\left\langle \left(\frac{dM}{dt}\right)_{tot} \right\rangle} = 0.1 \frac{M_{tot}}{\langle \tau_{tot} \rangle}$$

With this simulation, we cannot conclude on a value for t_a, as we only have a confidence interval for $\langle \tau_{tot} \rangle$. However, we can conclude on a lower limit for t_a, given by the highest value of the confidence interval ($\langle \tau_{tot} \rangle = 5.2 \cdot 10^{17}$). In our case, $t_a > 63 \ years$. With this simulation, we can conclude that the total AAM would be affected by less than 10 % in a 60 year long simulation. This is a quite poor constraint, as simulations for climate predictions are usually run on a hundred of years.
Therefore, we conducted a 12 000 days ($\approx$ 30 years) simulation, in order to obtain a stronger constraint. The empirical means (μ) and standard deviations (σ) obtained with this 12 000 days simulation are :

- $\mu_{tot} = -4.8 \cdot 10^{14}$, $\sigma_{tot} = 6.74 \cdot 10^{18}$ for the total torques.
- $\mu_{dyn} = 2.75 \cdot 10^{17}$, $\sigma_{dyn} = 5.27 \cdot 10^{17}$ for the torques from the dynamics.
- $\mu_{phys} = -2.75 \cdot 10^{17}$, $\sigma_p = 6.79 \cdot 10^{18}$ for the torques from the parametrizations.
- $\mu_{dissip} = -2.95 \cdot 10^{13}$, $\sigma_{dissip} = 1.86 \cdot 10^{14}$ for the torques from the dissipation.

The corresponding confidence interval obtained are :

$$\langle \tau_{tot} \rangle \in \begin{cases} [-1.25, 1.24] \cdot 10^{17} \ (CLT) \\ [-1.22, 1.22] \cdot 10^{17} \ (BTS) \end{cases}, 0 \in I_c$$

$$\langle \tau_{dyn} \rangle \in \begin{cases} [2.65, 2.85] \cdot 10^{17} \ (CLT) \\ [2.66, 2.85] \cdot 10^{17} \ (BTS) \end{cases}, I_c > 0$$

$$\langle \tau_p \rangle \in \begin{cases} [-4.0, -1.5] \cdot 10^{17} \ (CLT) \\ [-3.99, -1.52] \cdot 10^{17} \ (BTS) \end{cases}, I_c < 0$$

$$\langle \tau_{dissip} \rangle \in \begin{cases} [-3.26, -2.65] \cdot 10^{13} \ (CLT) \\ [-3.26, -2.65] \cdot 10^{13} \ (BTS) \end{cases}, I_c < 0$$

The size of the confidence interval is approximately divided by 3, as there are 10 more values in the simulation (n = 12 000 days instead of 1 200 days) and $\sqrt{(10)} \approx 3.2$. With this 12 000 days simulation, one cannot either conclude on a positive or negative tendency coming from the total torques as $0 \in I_c(\langle \tau_{tot} \rangle)$. However, as the interval size is narrower it is possible to have a more precise lower value for t_a : $t_a = 253$ years.
With this simulation we can conclude that the atmosphere will not significantly gain or loose momentum (by more than 10%) in a 250 years simulations.

It is also possible to conclude that the parametrized torques have a negative long term average, as the entire confidence interval for the expected value is lower than zero : $I_c(\langle \tau_p \rangle) < 0$.
This is the sign that an adjustment from the surface winds is taking place, in response to the spurious AAM source coming from the dynamical torques. Indeed, according to eq. (2.3.2), one should have $\langle \tau_p \rangle = 0$ over the steady state in a simulation without numerical errors. However, in the present case, $\langle \tau_p \rangle < 0$. As $\tau_p = \int_V \rho a cos(\phi) (\frac{du}{dt})_s \ dV$, this shows that the surface winds are different from what it would have been in a simulation without numerical errors.

Fig. 2.19 represents the integral of either the total torques, which corresponds to the computed AAM ($AAM(t) = AAM(t=0) + \int_{t=0}^{t} \tau_{tot}(t')dt'$), in purple, and the integral of the parametrized torques ($AAM(t=0) + \int_{0}^{t} \tau_p(t')dt'$), in green. The total AAM seems quite stable, which is coherent with the previously calculated interval for $\langle \tau_{tot} \rangle$: there might be a long term increasing or decreasing tendency of the total AAM (purple curve), but it is not detectable with this simulation. On the contrary, there is a clear decreasing tendency for the integral of the parametrized torques (green curve), due to the negative value of $\langle \tau_p \rangle$.
The reason of this balance between the positive trend in the numerical torques and the negative trend in the physical parametrization torques remains unclear.

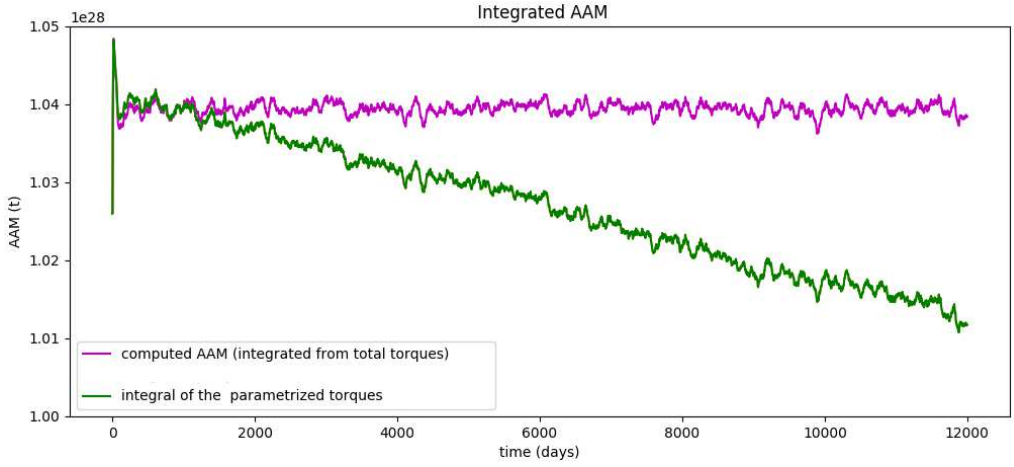

FIGURE 2.19 – Plot of the computed AAM (purple), and the integral of the parametrized torques (green) over the 12 000 days simulation.

It would be interesting to quantify the wind difference caused at the surface by this adjustment, and to quantify its impact on the general circulation.

2.4 Influence of the addition of a sponge layer

To study the influence of the addition of a sponge layer, a simulation with the same parameters as the baseline simulation but with an additional sponge layer on the last model levels, was carried out. This simulation is referred to as the **sponge - 39 llm** simulation, as there are 39 vertical levels (as in the baseline simulation).

2.4.1 Influence on the general circulation

The addition of a sponge layer in the model does affect the levels next to the top, as the winds are damped to zero.
The part with $P < 1 \cdot 10^5$, i.e $\sigma = p/p_s < 0.1$ (higher altitude) is affected by the presence of the sponge layer. The winds are damped to zero, while they were not in the absence of the sponge, leading to zonal wind differences between the two simulations, represented by the black contours in Fig. 2.20.
However, the bottom of the wind field is not affected at all. For $\sigma = p/p_s > 0.1$ the differences between the zonal winds of the two simulations is lower than $2\ m \cdot s^{-1}$.
In particular, the two jets are identical (the differences are lower than $2\ m \cdot s^{-1}$).

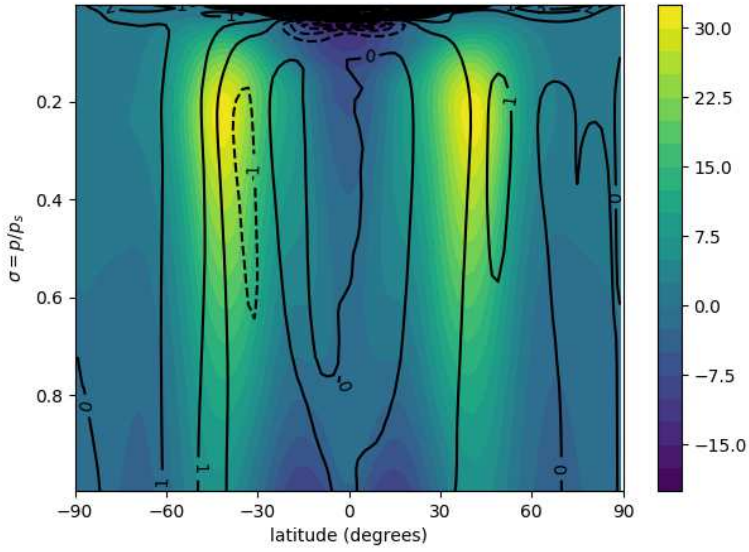

FIGURE 2.20 – The colors represent the zonal mean zonal wind of the baseline simulation (without sponge layer), and the black contours the difference between the wind fields of the baseline simulation and the sponge - 39 llm simulation. The data is averaged over days 200-1200.

2.4.2 Influence on the AAM budget

The main difference in the AAM budget between the simulation with and without sponge layer occurs in the dissipation torques. Indeed, in the baseline simulation (without a sponge layer), the spurious contribution to the AAM from the dissipation is negligible (four order of magnitude smaller than the physical contributions).
However, this is not the case anymore with the addition of a sponge layer, as one can see in comparing Fig. 2.21 and Fig. 2.22 representing the different torques in the baseline and sponge-39 llm simulations : the torques due to the dissipation (blue curve) become of order 10^{18} with the addition of a sponge layer.

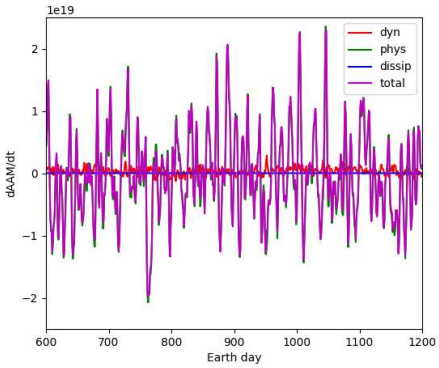

FIGURE 2.21 – torques : simulation without sponge layer

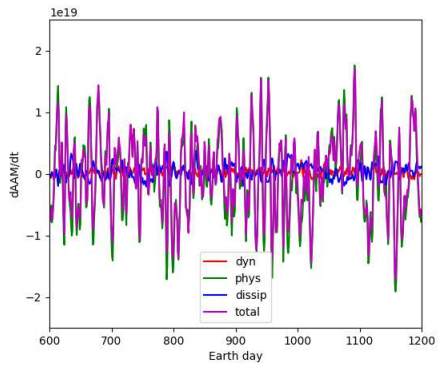

FIGURE 2.22 – torques : simulation with sponge layer

As a consequence, and differently from the baseline simulation without sponge layer, the indicators vary when considering the torques due to the dynamics only (second column of Table 2.2, $\alpha = dyn$) or to the dynamics and the dissipation (last column of Table 2.2, $\alpha = \epsilon = dyn+dissip$). The dissipation does affect the AAM budget.

	$\alpha = \text{dyn}$	$\alpha = dissip$	$\alpha = \epsilon = dissip + dyn$
$\frac{\int_{t_0}^{tss} \tau_\alpha \ dt'}{\int_{t_0}^{tss} \tau_{tot} \ dt'}$	-0.037	-0.063	-0.1
$\frac{\int_{t_0}^{tss} \tau_p \ dt'}{\int_{t_0}^{tss} \tau_{tot} \ dt'}$	1.1	-	-
$\frac{\sigma_\alpha}{\sigma_{tot}} \ (SS)$	0.08	0.18	0.21
$\frac{\sigma_p}{\sigma_{tot}} \ (SS)$	1.1	-	-
$r^2(\tau_\epsilon, \tau_{tot})$	0.09	0.6	0.51
$r^2(\tau_p, \tau_{tot})$	0.993	-	-

TABLE 2.2 – Different indicators of the quality of the AAM budget for the sponge - 39 llm simulation.

However, most of the AAM injected during the transient part still comes from the parametrized torques, as $\frac{\int_{t_0}^{tss} \tau_\epsilon \ dt'}{\int_{t_0}^{tss} \tau_{tot} \ dt'} = -0.1$ and $\frac{\int_{t_0}^{tss} \tau_p \ dt'}{\int_{t_0}^{tss} \tau_{tot} \ dt'} = 1.1$. The relative importance of the numerical torques in the AAM variations is stronger in the sponge - 39 llm simulation than in the baseline, but the parametrized torques still dominate the total AAM variations, as $\frac{\sigma_\epsilon}{\sigma_{tot}} = 0.21$ and $\frac{\sigma_p}{\sigma_{tot}} = 1.1$ during the steady state. The determination coefficient $r^2(\tau_p, \tau_{tot})$ remains very close to one. The indicators $\frac{\int_{t_0}^{tss} \tau_\epsilon \ dt'}{\int_{t_0}^{tss} \tau_{tot} \ dt'}$, $\frac{\int_{t_0}^{tss} \tau_p \ dt'}{\int_{t_0}^{tss} \tau_{tot} \ dt'}$, $\frac{\sigma_\epsilon}{\sigma_{tot}}$ and $\frac{\sigma_p}{\sigma_{tot}}$ were calculated for different steady state values : 80, 100 and 200 days. They did not vary (up to the digit considered here) : the choice of the steady state start does not impact the analysis.

2.5 Influence of the vertical resolution

We carried out an additional simulation with an higher vertical resolution. The amount of vertical levels (llm) was increased from 39 (baseline simulation) to 79. In this simulation, a sponge layer at the top was also used. This simulation is referred to as the **sponge - 79 llm** simulation.
The same indicators as in the previous sections were calculated. Compared to the simulation with sponge and 39 llm (Table 2.2), the indicators for the simulation with sponge and increased vertical levels (Table 2.3) indicates a better AAM budget quality. The influence of the dynamics is quite similar in both cases (the indicators are similar), except in the transient where the increased vertical resolution leads to a reduced impact from the dynamics.
The influence of the dissipation decreases as the vertical resolution is increased, as $\frac{\sigma_\epsilon}{\sigma_{tot}} = 0.1$ with the increased vertical resolution, compared to 0.21 previously, and $\frac{\int_{t_0}^{tss} \tau_\epsilon \ dt'}{\int_{t_0}^{tss} \tau_{tot} \ dt'} = 0.005$, compared to -0.1 previously.
This seems coherent. Indeed, as stated in Section 1.4 the contribution from the sponge layer is given by :

$$S = \int_V \rho a cos(\phi) (\frac{du}{dt})_{Sp} \ dV \tag{2.2}$$

with $(\frac{du}{dt})_{Sp}$ the wind variations due to the sponge layer :

$$(\frac{du}{dt})_{Sp} = \begin{cases} -k_{Sp}(p) \cdot u \quad for \ the \ 4 \ top \ levels, p < p_{sp} \\ 0 \ elsewhere \ (k_{Sp}(p) = 0 \ for \ p > p_{sp}) \end{cases} \tag{2.3}$$

with p_{sp} the highest pressure at which the sponge is applied (as it is only applied on the four last levels at the top i.e. at the lowest pressures).

	$\alpha = \text{dyn}$	$\alpha = dissip$	$\alpha = \epsilon = dissip + dyn$
$\frac{\int_{t_0}^{t_{ss}} \tau_\alpha \ dt'}{\int_{t_0}^{t_{ss}} \tau_{tot} \ dt'}$	-0.003	0.009	0.005
$\frac{\int_{t_0}^{t_{ss}} \tau_p \ dt'}{\int_{t_0}^{t_{ss}} \tau_{tot} \ dt'}$	0.994	-	-
$\frac{\sigma_\alpha}{\sigma_{tot}} \ (SS)$	0.08	0.07	0.11
$\frac{\sigma_p}{\sigma_{tot}} \ (SS)$	1.03	-	-
$r^2(\tau_\epsilon, \tau_{tot})$	0.08	0.55	0.19
$r^2(\tau_p, \tau_{tot})$	0.998	-	-

TABLE 2.3 – Different indicators of the quality of the sponge - 79 llm simulation

As $dV = r^2 dr cos(\phi) d\phi d\lambda$, $r \sim a$ (shallow atmosphere) and $-\frac{1}{g} dp \sim \rho dr$ (hydrostatic balance), the integral of eq. (2.2) can be written as :

$$S = \frac{a^3}{g} \int_\phi \int_\lambda \int_{p<p_{sp}} k_{sp}(p) \ (cos(\phi))^2 \ u(t, p, \phi, \lambda) d\phi d\lambda dp \tag{2.4}$$

In the simulations with 39 llm, the dissipation torques are negligible when no sponge is used, whereas they are of order $10^{18} kg \cdot m^2 \cdot s^{-2}$ when a sponge layer is added. Even if the contributions from the explicit diffusion operators (D) and the sponge layer (S) cannot be distinguished with our setup as it is only possible to access to the sum of the two, $(\frac{dM}{dt})_{dissip} = \tau_{dissip} = D + S$, this suggests that most of the dissipation torques come from the sponge layer torques in this configuration.
In the case of a higher vertical resolution (79 llm), the levels on which the sponge are applied (last four levels) correspond to a lower portion of the model, than in the case of a lower vertical resolution, as schematized in Fig. 2.23. This could explain that the torques due to the sponge layer (S) are lower in that case, and therefore that the torques due to the dissipation are also lower.

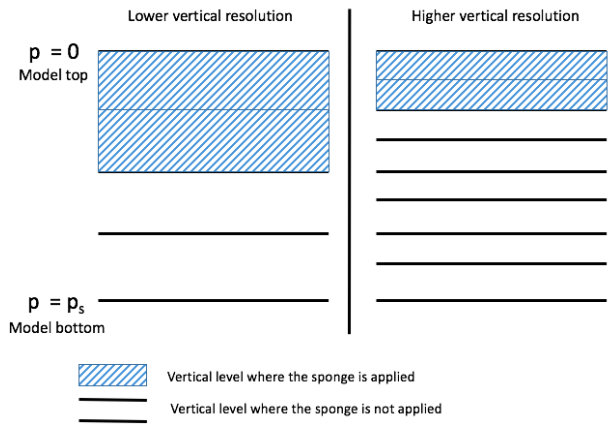

FIGURE 2.23 – Schematic representation of the vertical levels when a sponge is applied on the last two levels, with a higher vertical resolution on the right than on the left. In the case of a higher resolution, the portion of the model where the sponge is applied is less important in comparison to the simulation with lower vertical resolution.

2.6 Conclusion for the Held Suarez test case

To summarize the outcomes of this section :

- The circulation obtained in the baseline simulation is close to the one obtained in the Held and Suarez paper [8].
- The AAM budget is satisfying in the baseline simulation : the dissipation torques are completely negligible, the dynamical torques are fairly small, and most of the AAM content and fluctuations is due to the parametrized torques.
- An adjustment of the surface winds is taking place to balance the positive tendency coming from the numerical torques.
- The addition of a sponge layer in the model slightly alters the AAM budget, as the dissipation torques are not negligible anymore. The budget remains satisfying, as most of the AAM content and fluctuations is due to the parametrized torques.
- An increased vertical resolution decreases the magnitude of the dissipation torques, leading to a better AAM budget quality.

3

Modeling the Venusian atmosphere

3.1 The atmosphere of Venus

3.1.1 Available data on Venus

Although Venus is often seen as the sister of the Earth in terms of planetary properties, their atmospheres differ widely. The Venusian atmosphere is characterized by a very high surface pressure (92 bars) and a hot and dry surface ($\approx$ 735 K). The pressure and temperature decreases to 0.03 mbar and 175K at 100 km of altitude. The Venusian atmosphere is mainly composed of CO_2 (96.5 %) and N_2 (3.5 %). It has been first observed in 1962 with the Mariner 2 Probe but available data are still limited. However, the different space missions have allowed to determine certain features of Venus atmospheric circulation. A cloud layer is observed between 50-70 km, with strong retrogrades wind (in the same direction as the planetary rotation, which is the opposite of the Earth) of $\approx 100\ m \cdot s^{-1}$ from 50 $^\circ$N to 50 $^\circ$S, and decreasing toward the poles. The superrotation (winds going faster than the planetary rotation) extends from the surface to the cloud top [17]. However, the mechanisms maintaining the superrotation are still unknown.
The meridional circulation is driven by one Hadley cell in each hemisphere. In opposition to the Earth's atmosphere, they are not limited to the equatorial region. The extent of the Hadley cells is still unknown [16]. Observations seem to indicate that they do not extend to the poles and descend around 65 $^\circ$.
Thermal tides and momentum transport seem to play an important role in the venusian circulation.

	Venus	Earth
Mass	4.87×10^{24} kg	5.98×10^{24} kg
Radius	6052 km	6378 km
Density	5250 kg/m^3	5520 kg/m^3
Av. distance from Sun	108 million km	150 million km
Rotation period (day)	243 Earth days (retrograde)	23 hours 56 minutes
Orbit period (year)	224.7 Earth days	365.2 days
Surface temp. (mean)	465°C	15°C
Surface pressure	90 bar	1 bar (sea level)
Albedo	0.76	0.37
Highest point on surface	Maxwell Montes (8 km)	Mount Everest (8.8 km)
Orbit inclination	3.4°	0° by definition
Obliquity of axis	178°	23.5°
Moons	None	1 (The Moon)

FIGURE 3.1 – Main parameters for Earth and Venus (Copyright ESA)

Species	Venus	Earth
Carbon dioxide	0.96	0.0003
Nitrogen	0.035	0.770
Argon	0.00007	0.0093
Neon	0.000005	0.000018
Water vapor	0.000030	~.01
Sulfur dioxide	0.00015	0.2 ppb
Carbonyl sulfide	0.000004	
Carbon monoxide	0.00004	0.00000012
Atomic oxygen	trace	trace
Hydroxyl	trace	trace
Atomic hydrogen	trace	trace

FIGURE 3.2 – Composition. Picture from [19]

3.1.2 The importance of AAM conservation in the case of Venus

In 2012, in the framework of an International Space Science Institute working group, a comparison of six existing Venus General Circulation Models (GCM) was performed in [22]. The modeling

conditions (physical parametrizations, topography, boundary conditions etc) were choosen to be identical (as far as possible), in order to have comparable results. However, the results obtained differ widely, and large differences are obtained in the zonal mean zonal wind and the speed of the jets, as can be seen in Fig. 3.3.

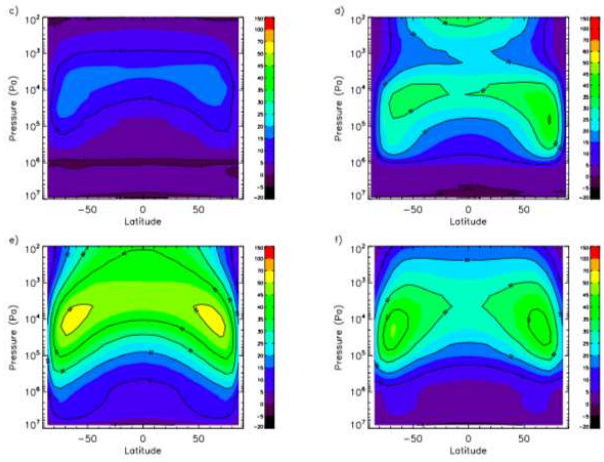

FIGURE 3.3 – Picture from [22], showing the wide disparity obtained in the results (here, the zonally and temporally averaged zonal wind fields obtained for different GCM)

A particularity of the Venusian atmosphere is that it is superrotating : the winds are faster than the planetary rotation. For example, the upper cloud layer accessible to visible wavelengths rotates with a period of approximately 4 days, whereas the solid rotation of Venus has a period of 243 days [3].
S. Lebonnois made the hypothesis that the wide differences obtained in the results in the intercomparison project ([22]) were due to AAM conservation defaults in the GCM [10].

3.2 Reference configuration for the modeling of Venus atmosphere : the "ISSI configuration"

3.2.1 Description of the test case

The vast majority of the GCM used to model the Venusian atmosphere are adapted from Earth's GCM, and most of the model use simplified physical and radiative parametrizations. In the idealized Venus configuration, as defined in [11], [12], used in the intercomparison project (ISSI) [22], and usually referred to in the literature as the "ISSI configuration", the parametrizations are simplified, in a way similar to the Held Suarez test case [8]:

- Temperatures are relaxed toward a prescribed, zonally symmetric "radiative equilibrium" $T_{eq}(P, \phi)$.

$$\frac{\partial T}{\partial t} = ... - k_T(T - T_{eq}(\phi, p))$$

This "radiative equilibrium" depends on latitude and pressure (and therefore, height).

$$T_{eq}(\phi, p) = T_{ref}(p) + T_1(p)(cos(\phi) - C)$$

T_{ref} is chosen following a reference temperature profile ([18]), and $T_1(p)$ is a perturbation term giving the peak equator-to-pole difference. Its profile was chosen to reflect Venusian conditions, and especially the peak in absorption of solar insolation in the cloud deck ([11]). It is represented in Fig. 3.4.

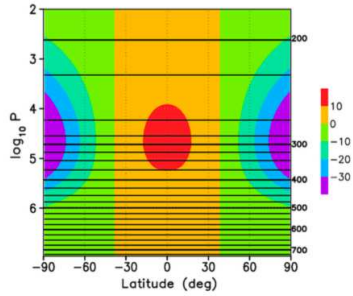

FIGURE 3.4 – Latitude-pressure distributions of $T_1(p)(cos(\phi) - C)$ (K, color shading) and $T_{ref}(p)$(K, contours). Figure from [26]

- The low-level winds are damped using a Rayleigh damping, in order to represent boundary-layer friction.

$$\frac{\partial \mathbf{u}}{\partial t} = ... - k\mathbf{u}$$

  with k (s^{-1}) the damping coefficient, equal to zero outside the first vertical levels of the mesh.

- Additionnaly, a sponge layer is implemented in the last vertical levels of the model. This sponge layer damps the horizontal velocity to zero.

The specific heat is taken as constant, Cp = 1000 J/kg/K, except when specified otherwise. A flat topography is used, and no diurnal or seasonal variation in the forcing or dissipation are implemented. The atmosphere is at rest in the initial condition. In this setup, as in the Held Suarez setup, the only parametrized physical sources or sinks of AAM come from the surface friction, through the Rayleigh damping of surface winds (first vertical level near the ground).

3.2.2 Limitations due to the test case

The limitations due to the test case are mainly the same as in the Held Suarez setup. Again, the only parametrized source or sink of AAM depends on the surface friction, and therefore the surface winds, which can be affected by numerical errors.
Another limitation is the heavy computational load of idealized Venus simulations. At nbp = 30 (the highest resolution used during this thesis for Venus simulations), one needs approximately 3 days of simulation to compute 150 Venus days (17 550 Earth days). As a comparison, when using the same amount of processors, Held Suarez simulations needed only 20 hours to compute 12 000 Earth days, with a higher resolution (nbp = 40).

3.3 Reference simulation

Our reference simulation was chosen in order to be easily comparable with the simulations run by S. Lebonnois with LMDZ. Therefore, the parameters were chosen identical, and the horizontal resolution was set accordingly.
The parameters for the baseline simulation are :

- nbp = 30
- the vertical levels are defined in the same way as in the ISSI intercomparison ([22]). There are 50 vertical levels.
- The explicit diffusion operator are of second order, with a time constant equal to t_{dissip}=10 000s.

3.3.1 General circulation

The general circulation obtained with the baseline configuration is represented in Fig. 3.5. The maximum zonal winds are around 30 $m \cdot s^{-1}$. The highest zonal velocities are quite stable around P = 10^4 : the latitudinal velocity gradient is small. Around latitudes from 60 ° to 90 °, there are quite high velocities at higher pressures (lower altitudes). The thermal wind relation for cyclostrophic balance (eq. (3.1)) seems to be qualitatively quite well verified.

$$2u\frac{\partial u}{\partial \xi} = -\frac{R}{tan(\phi)}(\frac{\partial T}{\partial \phi})_{p=const} \tag{3.1}$$

with $\xi = -ln(\frac{p}{p_{ref}})$, p_{ref} the surface pressure, R the gas constant, T the temperature and ϕ the latitude. ξ is increasing with altitude as the pressure is decreasing. A decrease (increase) of temperature toward the poles corresponds to an increase (decrease) of the zonal wind velocity with altitude. For more details on the thermal wind equation, see Section 5.2.
The meridional circulation (black contours of Fig. 3.5) is composed of two dominant Hadley cells (one in each hemisphere), and polar reversed circulations.
The temperature contrast is low. In the cloud layer, around $3 \cdot 10^4$ Pa, the temperature contrast at the poles is equal to 1.4 K and -1K at the equator, corresponding to 2-3 K of equator-pole temperature difference. This corresponds to the pressure level where the imposed temperature contrast (depicted in Fig. 3.4) is the highest with approximately 40 K of difference between the equator and the pole : the temperature contrast obtained is much weaker than the imposed one, that would take place if the winds velocity were equal to zero everywhere in the atmosphere. At the surface, the equator-pole difference is approximately equal to 5K. In comparison, in the Held Suarez test case the equator-pole temperature difference is around 50 K.

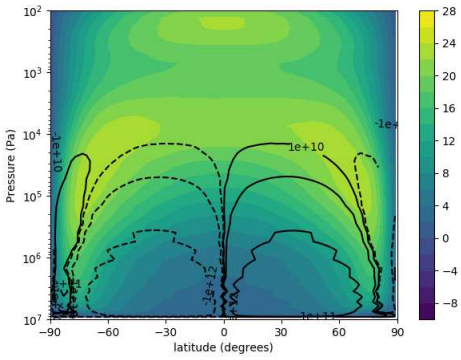

FIGURE 3.5 – The colors represent the zonal mean zonal wind (m/s), the black contours represent the streamlines.
Averaged over Venus days = 200 - 300

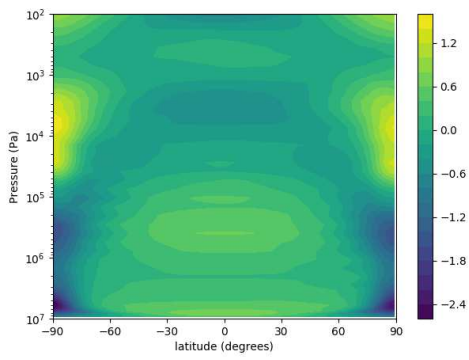

FIGURE 3.6 – Temperature contrast (K)

Averaged over Venus days = 200 - 300

3.3.2 Angular momentum budget

Total, wind, mass and normalized AAM

The simulation is considered to have reached a steady state at approximately 150 Venus days. The normalized AAM (total AAM divided by mass AAM), represented in the right panel of Fig. 3.7 is not varying by more than 5 % around the mean value from that day on. At the start of the simulation, the atmosphere is at rest, so the wind AAM is equal to zero. It increases to reach a value approximately 3 times higher than the mass AAM, as visible in the left panel of Fig. 3.7. This is a completely different configuration from the Held Suarez test case where the total AAM was mainly composed of the mass AAM, and the wind AAM was only a small portion of it.
During the steady state, the mean value of the wind AAM is equal to $1.12 \cdot 10^{28}$ $kg \cdot m^2 \cdot s^{-1}$,

and its standard deviation is equal to $3.7 \cdot 10^{26}\ kg \cdot m^2 \cdot s^{-1}$. The mean value of the mass AAM is $3.49 \cdot 10^{27}\ kg \cdot m^2 \cdot s^{-1}$, and its standard deviation is of order $10^{22}\ kg \cdot m^2 \cdot s^{-1}$. The mean value of the total AAM is $1.47 \cdot 10^{28}\ kg \cdot m^2 \cdot s^{-1}$, and its standard deviation is equal to $3.7 \cdot 10^{26}$ $kg \cdot m^2 \cdot s^{-1}$.

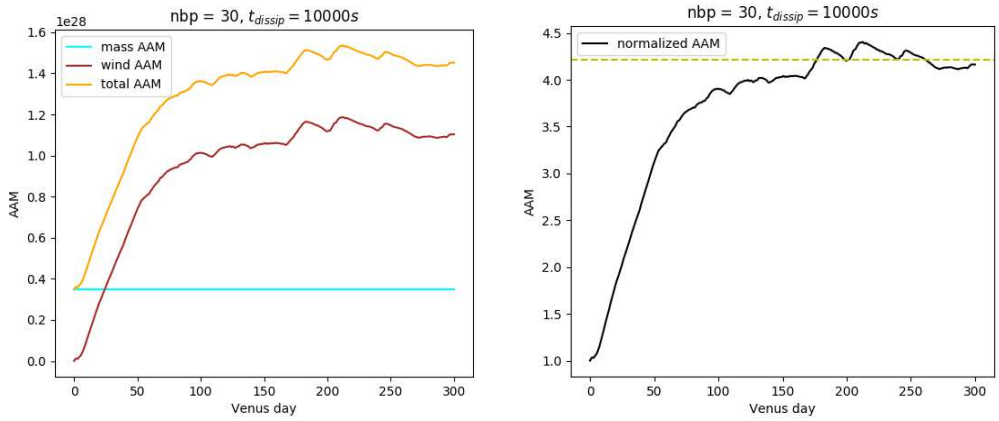

FIGURE 3.7 – mass, wind, total and normalized AAM of the baseline simulation. The yellow dashed line represents the mean normalized AAM value from 150 Venus days to the end of the simulation. From 150 Venus days onward, the normalized AAM is not varying by more than 5 % around this mean value.

Torques

The torques affecting the AAM over the simulation are represented in Figs. 3.8 and 3.9 : the torques due to the dynamics (red curve), the torques due to the physical parametrizations (green curve), the torques due to the dissipation (blue curve) and the total torques, sum of the 3 previous torques (purple). There is a spin-up phase, where the atmosphere is gaining angular momentum : in the first 100 Venus days, the total torques are always positive.

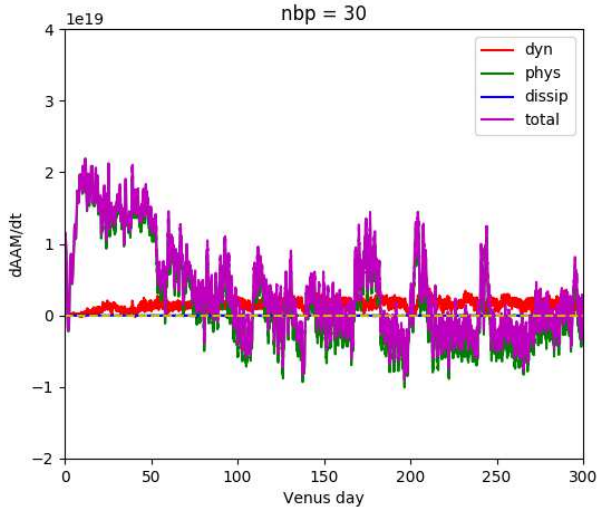

FIGURE 3.8 – Torques due to the dynamics (red), the parametrization (green), and the dissipation (blue, cannot be distinguished from the zero yellow dashed line). Total torques in purple.

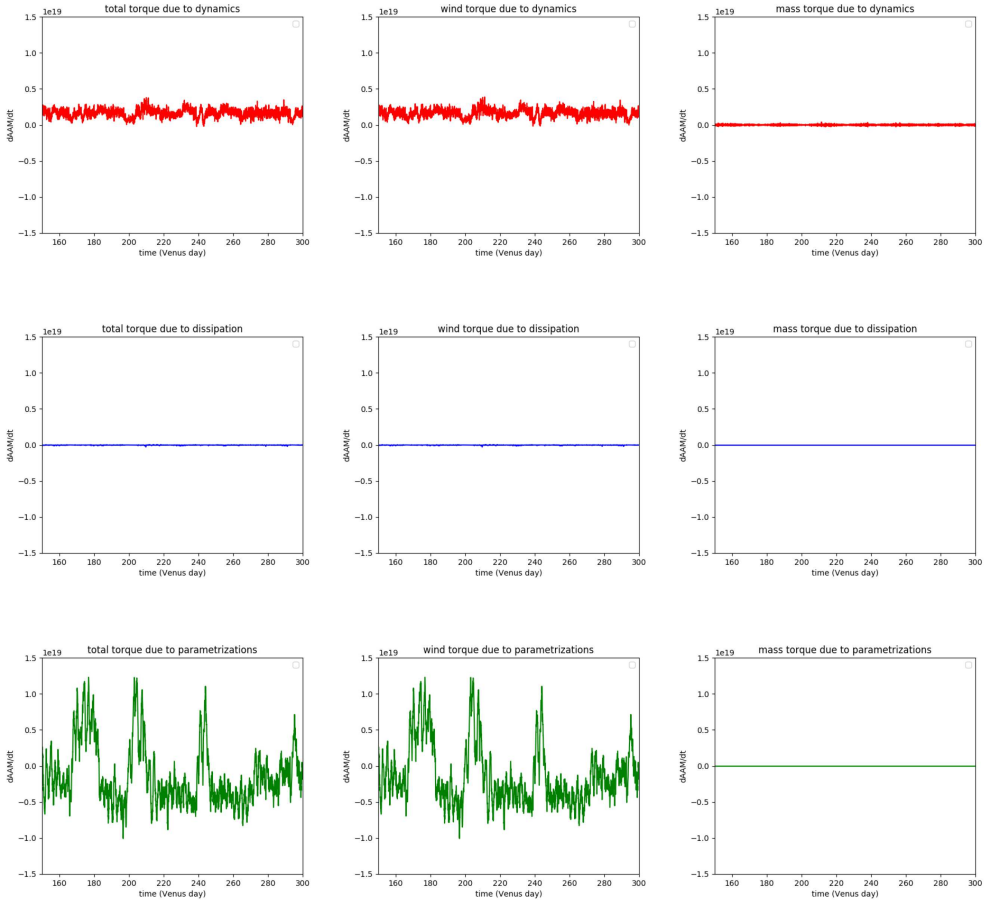

FIGURE 3.9 – First row : torques due to the dynamics. Second row : torques due fo the dissipation. Third row : torques due to the physical parametrizations.

The total torque curve mainly overlaps with the parametrized torques curve.
Fig. 3.9 represents the different torques as in Fig. 3.8 but splitted into the different contributions. The standard deviation of the parametrized torques during the steady-state is $4.2{\cdot}10^{18}\ kg{\cdot}m^2{\cdot}s^{-2}$. The torques coming from the dissipation (third row) are of order $10^{16}\ kg{\cdot}m^2{\cdot}s^{-2}$: $\tau_{dissip} << \tau_p$. The standard deviation of the dynamical torques, $5.4{\cdot}10^{17}\ kg{\cdot}m^2{\cdot}s^{-2}$, is one order of magnitude smaller than the standard deviation of the parametrized torques. The total dynamical torques (first row, first column), $\tau_{dyn} = (\frac{dM}{dt})_{dyn} = (\frac{dM_o}{dt})_{dyn} + (\frac{dM_r}{dt})_{dyn} = \tau_{mass\ dyn} + \tau_{vel\ dyn}$, is mainly driven by the $\tau_{vel\ dyn}$ (vel dyn torque) term (first row, second column). This is a major difference with the Held Suarez setup, where the total dynamical torque came from the imbalance between the $\tau_{mass\ dyn}$ and $\tau_{vel\ dyn}$ terms. The reason of this difference remains unclear.

Indicators of the AAM budget quality

The same indicators as in the Held Suarez Section 2.3.1 were calculated. A major difference is the indicators sensitivity to the choice of the value of the steady-state start. With the baseline Venus simulation, the choice of the value for the steady-state start does impact the computed indicators, as can be seen in Table 3.1. The transition from transient to steady-state is not as clear as in the Held Suarez case. In the following, we will take the value of 150 VD as the steady-state start.

	SS = 130 VD	SS = 150 VD	SS = 170 VD
$\frac{\int_{t_0}^{t_{ss}} \tau_\epsilon \ dt'}{\int_{t_0}^{t_{ss}} \tau_{tot} \ dt'}$	0.15 (0.15)	0.18 (0.18)	0.21 (0.21)
$\frac{\int_{t_0}^{t_{ss}} \tau_p \ dt'}{\int_{t_0}^{t_{ss}} \tau_{tot} \ dt'}$	0.85	0.82	0.79
$\frac{\sigma_\epsilon}{\sigma_{tot}} \ (SS)$	0.13 (0.13)	0.12 (0.13)	0.13 (0.13)
$\frac{\sigma_p}{\sigma_{tot}} \ (SS)$	0.999	0.998	0.997
$r^2(\tau_\epsilon, \tau_{tot})$	0.14	-	-
$r^2(\tau_p, \tau_{tot})$	0.993	-	-

TABLE 3.1 – Different indicators of the quality of the AAM budget for the reference simulation. The values in brackets correspond to when the dynamics only is considered in the numerical errors, without the dissipation.

The values in brackets in Table 3.1 correspond to the indicators value when only the dynamical torques are considered (and not the dissipation torques). One can see that the indicators computed by considering the numerical errors (dynamics and dissipation) or the dynamics only are equal : the dissipation has a negligible role.

During the simulation start, most of the AAM gained by the atmosphere comes from the parametrized torques, as the parametrized and total torques overlap significantly (visible in Fig. 3.8) : $\frac{\int_{t_0}^{t_{ss}} \tau_p \ dt'}{\int_{t_0}^{t_{ss}} \tau_{tot} \ dt'} = 0.82$, so approximately 80 % of the AAM content comes from the parametrized torques.

During the steady-state, the AAM fluctuations are mostly dominated by the parametrized torques, as $\frac{\sigma_\epsilon}{\sigma_{tot}} = 0.13$.

Statistical Analysis of the torques

Fig. 3.10 represents the integral of the total torques, which corresponds to the computed AAM ($AAM(t) = AAM(t=0) + \int_{t=0}^{t} \tau_{tot}(t')dt'$) and the integral of the parametrized torques ($AAM(t=0) + \int_{0}^{t} \tau_{p}(t')dt'$). The total AAM (purple curve) seems to have a small increasing tendency, suggesting that the total torques have a non zero mean during the steady-state.

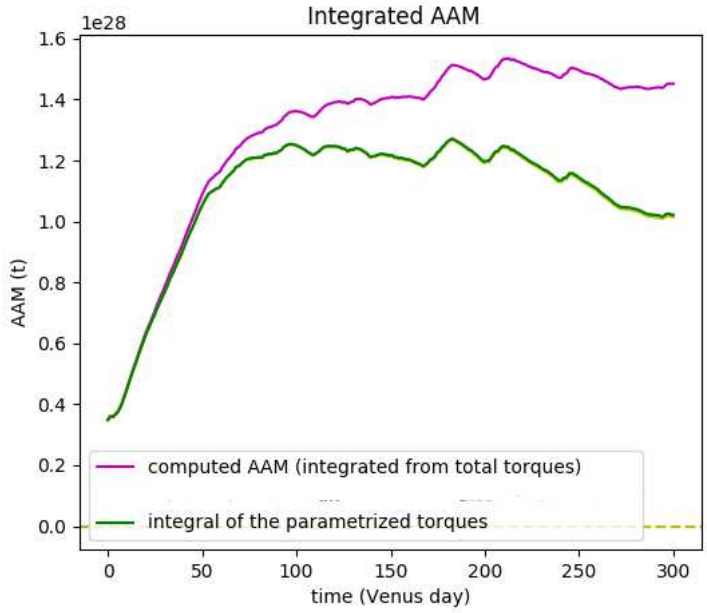

FIGURE 3.10 – Evolution of the computed AAM over the simulation (blue dashed line). The integral of all the torques (numerical and parametrized), is represented by the red dashed line (entirely covered by blue) : this is the integral of the purple curve from the left panel. The integral of the physical torques (integral of the green curve of the left panel) is in cyan, and the integral from the physical and dissipative torques (integral of the green and blue curve of the left panel) is in orange.

To quantify this increase, we used the bootstrap method or the central limit theorem approximation, as in Section 2.3.1 in order to obtain a confidence interval of the expected value of the total torques $\langle \tau_{tot} \rangle$ during the steady-state. We suppose the torques follow a distribution of expected value m and finite standard deviation s.
Applied over the steady-state (from 150 Venus days onward), we obtain :

$$\langle \tau_{tot} \rangle \in \begin{cases} [2.14, 3.74] \cdot 10^{17} > 0 \\ [2.13, 3.75] \cdot 10^{17} > 0 \end{cases}$$

The AAM is still increasing during the steady state. Assuming that the global tendency would remain similar in the future of the simulation, one can approximate the time t_a at which the atmosphere will have gained 10 % more AAM.

$$t_a = 0.1 \frac{M_{tot}}{\langle \tau_{tot} \rangle} \in [370,\ 647]\ Venus\ days$$

The total AAM is still slightly increasing during the steady state, however it has been estimated that its mean value would not increase by more than 10 % in the next 300 Venus days of simulation, if the tendency of the total torques remain the same.

3.4 Influence of the resolution and dissipation

Additionally to the baseline simulation, we carried out sensitivity simulation in order to study the influence of :

- the horizontal resolution (driven by the parameter nbp)
- the dissipation (driven by the dissipation timescale t_{dissip})

We performed two simulations with exactly the same parameters as in the baseline simulation, except with a lower horizontal resolution : nbp was set to 10 and 20 (called **nbp = 10** and **nbp = 20** simulations). We performed one simulation with exactly the same parameters as the baseline simulation, but with a higher dissipation time scale, t_{dissip} = 25 000s, corresponding to a lower dissipation (called $\mathbf{t_{dissip}}$ **= 25000s** simulation) .
In the case of Venus, 30 nbp corresponds to a characteristic size of the grid cells of 230 km. 20 nbp corresponds to 340 km, and 10 nbp corresponds to 680 km.
The nbp = 10 and nbp = 20 simulations were run for 500 Venus days, whereas the nbp = 30 simulations were run for 300 Venus days. The circulation obtained and averaged on the last 100 days of the simulations are plotted in Figs. 3.11, 3.12, 3.13 and 3.14. The circulation obtained by S. Lebonnois with LMDZ (with similar settings as the baseline simulation) in the simulation days 96-106 is plotted in the Appendix section 5, in Fig. 5.10.

3.4.1 General circulation

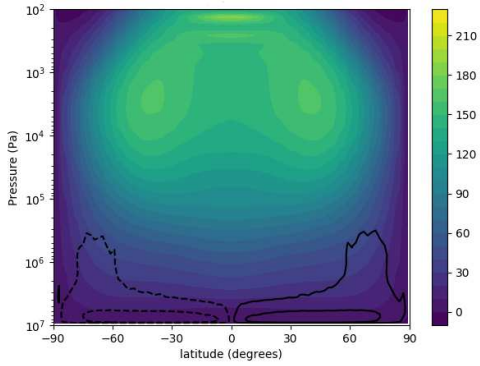

FIGURE 3.11 – nbp = 10

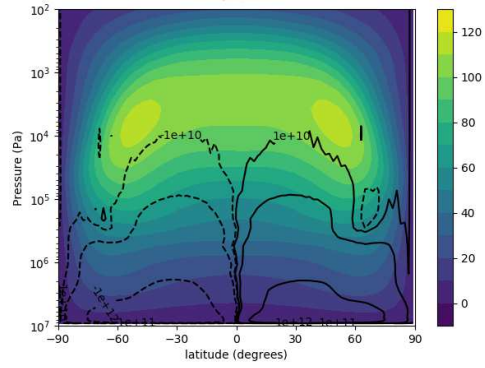

FIGURE 3.12 – nbp = 20

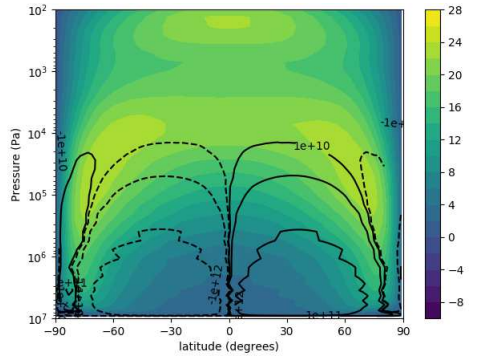

FIGURE 3.13 – nbp = 30, $t_{dissip} = 10000s$

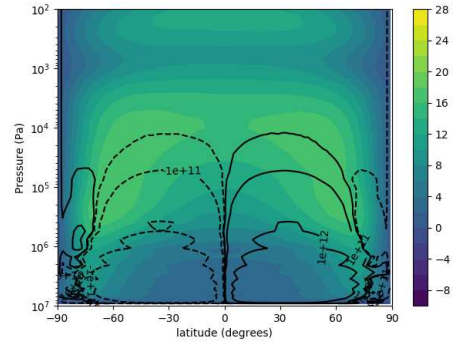

FIGURE 3.14 – nbp = 30, $t_{dissip} = 25000s$

The general circulation obtained differ widely when varying a parameter. The most important difference is obtained when the horizontal resolution is changed. Much higher zonal velocities

are obtained in the case nbp = 10 and nbp = 20 than in the nbp = 30 cases, with maximum velocities around 220 $m \cdot s^{-1}$ for nbp = 10 and 130 $m \cdot s^{-1}$ for nbp = 20.
The meridional circulation also differ widely. In the nbp = 10 and nbp = 20 cases, there are two dominant Hadley cells, but no reversed cells at the pole as in the nbp = 30 cases. In the nbp = 10 case, the Hadley cells are limited relatively close to the ground.
The meridional circulation for the two nbp = 30 cases are quite similar, with the presence of two dominant Hadley cells and indirect cells at the poles. However, the zonal winds differ, with maximum zonal winds around 20 $m \cdot s^{-1}$ in the $t_{dissip} = 25000s$ case and around 30 $m \cdot s^{-1}$ in the $t_{dissip} = 10000s$

3.4.2 Angular momentum budget

The evolution of the normalized AAM (total AAM divided by mass AAM) of each simulation is plotted in Fig. 3.15. The mass AAM is similar in all the simulation : the differences obtained in the normalized AAM come from differences in wind AAM. The wind AAM obtained in the nbp = 10 and nbp = 20 simulation is much higher than in the nbp = 30 simulations.

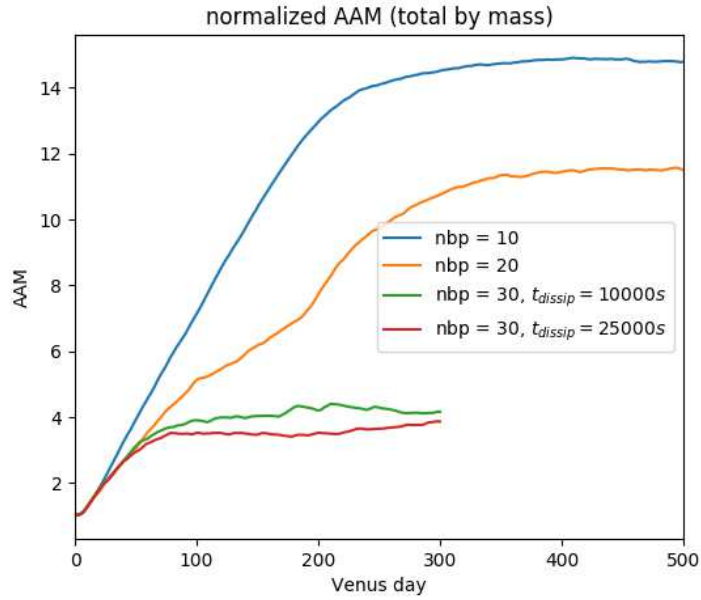

FIGURE 3.15 – Evolution of the normalized AAM of the different simulations.

The dynamical, dissipation, parametrized, and total torques for the different simulations are plotted in Figs. 3.16, 3.17, 3.18, 3.19. Graphically, one can see that the impact of the dissipation (blue curve) is mostly negligible in all the simulations, except the nbp = 10 simulation. The dynamical errors are much stronger and noisier in the lower resolution cases. The spin-up phase, with the total torques being above zero is longer in the lower resolution cases, where the statistical steady-state is reached around 250 Venus days for nbp = 10 and around 350 Venus days for nbp = 20.
The same indicators as previously were calculated and are summed up in Table 3.2.
When considering the steady-state part of the simulation, the indicators show a better AAM budget quality when the resolution is increased. The share of the total AAM fluctuations due to the fluctuations of the parametrized torques increases with increased resolution, as the indicator $\frac{\sigma_\epsilon}{\sigma_{tot}}$ decreases and $\frac{\sigma_p}{\sigma_{tot}}$ increases. The correlation coefficient of the total and parametrized torques also increases with increased resolution.
When considering the transient regime, the indicators show an increase in the AAM budget quality with increased resolution between nbp = 20 and nbp = 30.

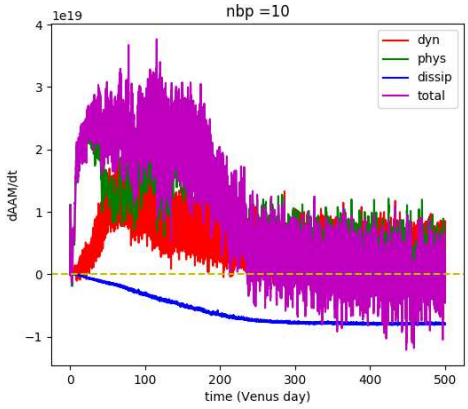

FIGURE 3.16 – nbp = 10

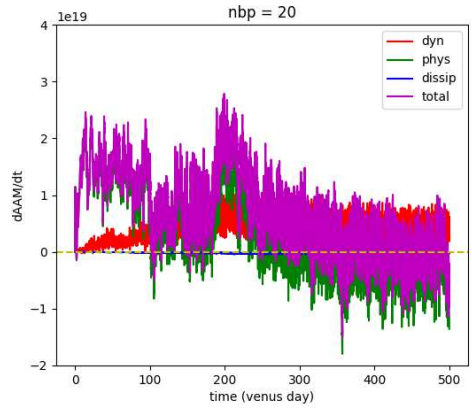

FIGURE 3.17 – nbp = 20

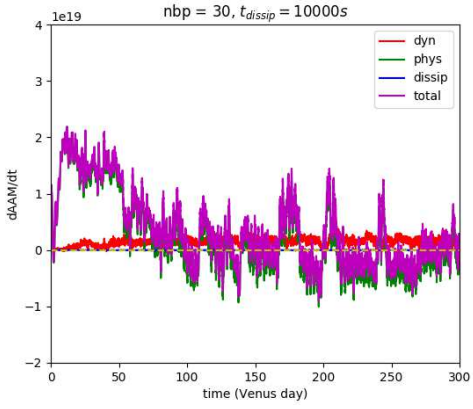

FIGURE 3.18 – nbp = 30, $t_{dissip} = 10000s$

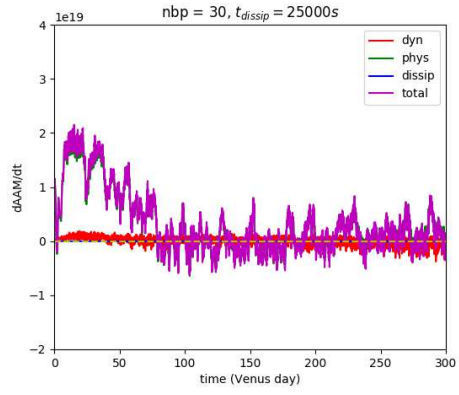

FIGURE 3.19 – nbp = 30, $t_{dissip} = 25000s$

However, the indicators $\frac{\int_{t_0}^{t_{ss}} \tau_\epsilon \ dt'}{\int_{t_0}^{t_{ss}} \tau_{tot} \ dt'}$ seem to indicate a better AAM conservation in the nbp = 10 case, which seems inconsistent with Figs. 3.16 and 3.17 : the dynamical torques (red curve) have a lower mean and standard deviation in the nbp = 20 resolution case, indicating a better AAM conservation than in the nbp = 10 case. This is due to the fact that with the indicator $\frac{\int_{t_0}^{t_{ss}} \tau_\epsilon \ dt'}{\int_{t_0}^{t_{ss}} \tau_{tot} \ dt'}$, one does not take into account the fluctuations occurring during the transient part of the simulation, which are "masked" by the integral, and only the mean value of the torques is taken into account. In the nbp = 10 case, the mean value of the dissipation and dynamical torques approximately balance each other, which leads to a value closer to zero for the indicator. This is also visible, as the indicator in brackets (when considering the dynamics alone) is higher, equal to 0.4, whereas the indicator for the total numerical errors is equal to 0.18. This shows that these indicators should always be considered carefully, with a regard to the dynamical and dissipation torques curves.

The quality of the AAM budget increases with increased resolution, as the AAM variations become relatively more driven by the parametrized torques than the numerical one. However, even with the highest horizontal resolution, the quality of the AAM budget is not as good as in the Held Suarez simulations.

The impact of the dissipation is not straightforward. The dissipation does not affect the AAM budget directly, as the indicators of the total numerical torques (dissipation + dynamics) and dynamics only (in brackets in Table 3.2) are equal for the nbp = 30 case. However, when using

	nbp = 10	nbp = 20	nbp = 30 t_{dissip} = 10000s	nbp =30 t_{dissip} = 25000s
$\frac{\int_{t_0}^{t_{ss}} \tau_\epsilon \ dt'}{\int_{t_0}^{t_{ss}} \tau_{tot} \ dt'}$	0.18 (0.4)	0.37 (0.39)	0.18 (0.18)	0.05 (0.05)
$\frac{\int_{t_0}^{t_{ss}} \tau_p \ dt'}{\int_{t_0}^{t_{ss}} \tau_{tot} \ dt'}$	0.82	0.63	0.82	0.95
$\frac{\sigma_\epsilon}{\sigma_{tot}}$ (SS)	0.56 (0.55)	0.33 (0.33)	0.13 (0.13)	0.26 (0.26)
$\frac{\sigma_p}{\sigma_{tot}}$ (SS)	0.84	0.97 (0.97)	0.999	0.98
$r^2(\tau_\epsilon, \tau_{tot})$	0.78 (0.5)	0.003 (0.005)	0.14 (0.14)	0.24 (0.24)
$r^2(\tau_p, \tau_{tot})$	0.84	0.95	0.993	0.987

TABLE 3.2 – Different indicators of the quality of the AAM budget for different simulations

different dissipation timescale for the explicit diffusion operators, it leads to different general circulation, which in turn affect the dynamical errors and the AAM budget quality. This is discussed in the next section.

3.5 Dependency from the dynamical errors to the general circulation.

From the simulations carried out during this thesis, it has been seen that the dynamical torques (and consequently the numerical errors) depend on the general circulation. Examples are given in this section.

We first consider the two nbp = 30 simulation. Except for the dissipation timescale (set to t_{dissip} = 10 000s or 25 000s respectively), these two simulations have exactly the same parameters. Their mean circulation in the last 100 days of the simulation are plotted in Figs. 3.13 , 3.14, and their respective torques are plotted in Figs. 3.18 and 3.19.

In these two cases, the meridional circulation (represented by the black streamlines in Figs. 3.13 , 3.14) is quite similar with two dominant Hadley cells and two reversed cells at the poles. However, their zonal circulation differ (the zonal mean zonal wind is represented in colors in Figs. 3.13 , 3.14) : the winds are lower in the simulation with a larger dissipation timescale.

As it has been seen in Table 3.2, their total numerical errors are driven by the dynamics, as the impact of the dissipation is negligible.

However, for these two simulations, the different indicators calculated differ. Furthermore, the mean value of the dynamical torques (μ_{dyn}) and its standard deviation (σ_{dyn}) estimated over the last 100 Venus days differ in these two simulations.

- $\mu_{dyn} = 1.62 \cdot 10^{18}\ kg \cdot m^2 \cdot s^{-2}$ and $\sigma_{dyn} = 5.6 \cdot 10^{17}\ kg \cdot m^2 \cdot s^{-2}$ for the t_{dissip} = 10 000s simulation
- $\mu_{dyn} = -4.09.62 \cdot 10^{17}\ kg \cdot m^2 \cdot s^{-2}$ and $\sigma_{dyn} = 7.46 \cdot 10^{17}\ kg \cdot m^2 \cdot s^{-2}$ for the t_{dissip} = 25 000s simulations

If we consider that the dynamical torques are following a distribution of expected value $\langle \tau_{dyn} \rangle$ and finite standard deviation, this gives a confidence interval for the expected value of the dynamical torques :

- $\langle \tau_{dyn} \rangle \in$ [1.60 , 1.64] $\cdot 10^{18}\ kg \cdot m^2 \cdot s^{-2}$ for the t_{dissip} = 10 000s simulation
- $\langle \tau_{dyn} \rangle \in$ [-0.43 , -0.39] $\cdot 10^{18}\ kg \cdot m^2 \cdot s^{-2}$ for the t_{dissip} = 25 000s simulation

These two confidence interval do not overlap. The expected value and standard deviation of the dynamical torques are different in these two simulations. The expected value of the dynamical torques is positive in one case, and negative in the other, and there is one order of magnitude of difference in their absolute value. In one case, the dynamical errors tend to inject angular

momentum in the atmosphere, whereas in the other it takes angular momentum from the atmosphere : the dynamical errors are of different nature. This shows that the nature of the dynamical errors depends on the general circulation. In that case, the different dissipation timescales lead to different circulations, which lead to different kind of dynamical errors.

Another example of the dependency of the dynamical torques to the general circulation could be obtained by considering two simulations with exactly the same physical constants and numerical parameters, but with two different imposed temperature contrasts. The obtained circulation and winds would differ (as the winds are linked to the temperature gradient, by the thermal wind relation), and the numerical errors would highly probably also be different.
Furthermore, with the current setup, different circulations lead to different parametrized torques, as they depend on the surface winds. In one case, the parametrized torques could be higher, thus reducing the relative share of the dynamical torques in the total torques.
During this thesis, due to technical reasons and lack of time, it was not possible to change the imposed temperature contrast to check this hypothesis. However, simulations with different thermodynamical parameters were carried out. We performed a simulation with exactly the same parameters as the baseline simulation, but with a different Cp, Cp = 887 J/kg/K. This simulation gave a different circulation, as well as different parametrized and dynamical torques (plotted in Figs 3.20 and 3.21). In this simulation, no steady-state is reached after 300 Venus days of simulation. The meridional circulation is only composed of two direct Hadley cells. There are no indirect polar cells. The zonal winds obtained are much stronger than in the baseline simulation (80 $m \cdot s^{-1}$, in comparison to 30 $m \cdot s^{-1}$)
In the last 100 Venus days of the simulation, the numerical torques have a standard deviation of $1.6 \cdot 10^{18}$ $kg \cdot m^2 \cdot s^{-2}$, which is approximately 3 times higher than in the baseline simulation. The AAM fluctuations are not mainly driven by the parametrized torques : $\frac{\sigma_\epsilon}{\sigma_{tot}} = 0.7$ and $\frac{\sigma_p}{\sigma_{tot}} = 0.7$. The determination coefficient between the total and parametrized torques in the last 100 Venus days of the simulation is equal to 0.51 and 0.48 between the dynamical and total torques. The quality of the AAM budget is poor, as the AAM variations are equivalently driven by the parametrized and numerical torques.
This was not the case in the baseline simulation, which had exactly the same numerical parameters and constants (except the thermodynamical one), but for which the general circulation was completely different. In addition, the standard deviation and mean value of the dynamical torques clearly changes between the simulations days 0-200 and 200-300, where the dynamical torques become more important at the end of the simulation (visible in Fig. 3.21). The only thing that has changed is the circulation, which is evolving in the simulation. This again shows that numerical errors, parametrized torques, and consequently the AAM budget quality depend on the general circulation.
In an intern note on the LMDZ model ([1]), F. Hourdin stated that the numerical errors depend on the circulation type. He found out that certain kind of circulation favoured numerical errors for the LMDZ GCM. During this thesis, it was not possible to find an explicit link between the circulation type and stronger or lower numerical errors with DYNAMICO. However we found that for different simulations with DYNAMICO with identical numerical parameters but characterized by different circulation, the numerical errors were of different magnitudes, or had different time averaged values.
This is an incentive for a systematic check of the AAM budget when considering different circulations : if a GCM has shown good AAM conservation properties and low numerical errors in a certain configuration, it does not mean that it will have satisfying AAM conservation properties if the general circulation changes.

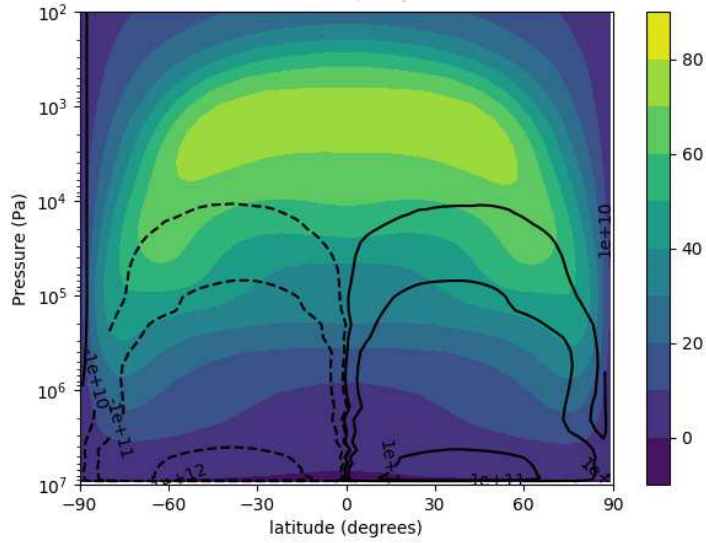

FIGURE 3.20 – zonal winds (color) and meridional streamfunction (black contours) for the Cp = 887 J/kg/K simulation, averaged over venus days 200-300

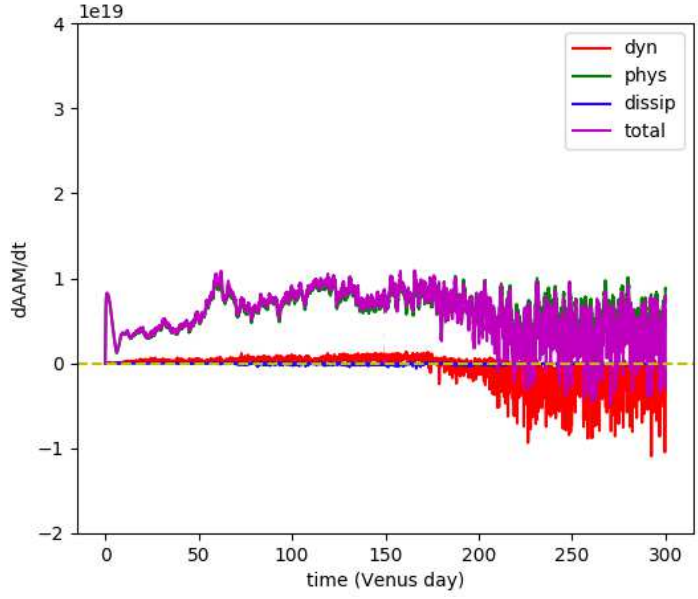

FIGURE 3.21 – Evolution of the AAM torques over the whole Cp = 887 J/kg/K simulation : dynamical torques (red), dissipation torques (blue), parametrized torques (green) and total torques (purple).

4

Conclusion

During this thesis, we investigated the modeling of the atmosphere of the Earth and Venus, using idealized configurations. We developed a methodology to look at the quality of the AAM budget, and applied it for idealized Earth and Venus configurations. The results show that the AAM budget is better in the Held Suarez test case than in the idealized Venus configuration, where numerical errors are more important. In the case of Venus, the quality of the AAM budget is increasing with increased horizontal resolution. It has been shown that numerical errors do not only depend on the numerical and modeling parameters chosen, but also on the general circulation itself. This implies that the quality of the AAM budget should be studied carefully for each simulation : if the AAM variations are mostly driven by the parametrized torques in a simulation with a certain circulation, it does not mean that it should be the case for any given circulation.

Consequently, if a GCM exhibits a satisfying angular momentum budget for the Held Suarez configuration, it does not necessarily imply that its angular momentum budget will be satisfying for an idealized Venus configuration.

Many questions remain open. The settings used do not permit to quantify the impacts on the circulation of these numerical errors. Due to the feedback existing between the numerical errors, the general circulation, and the physical parametrizations, one cannot know what the AAM content of the atmosphere would have been in a simulation without numerical errors.

In addition, the role of indirect polar cells in the general circulation should be further studied. Yamamoto and Takahashi suggested in their article [27] that poleward eddy heat fluxes could be a key driver determining the slow or fast super rotation state obtained in the cloud layer.

5 Appendix

5.1 Help for plots reading

The plots shown in this thesis for the general circulation are often zonal plots of time averages of the data. This mean that the data has been averaged over a certain time period (time average) and then averaged over longitude (zonal average).
This allows to represent a 4D array (depending on the time, the vertical level i.e. the pressure, the latitude and the longitude), into a 2D array (depending on pressure and latitude), and gives information about the mean circulation.
The x-axis of general circulation plots represents the latitude.
The y-axis, is either the pressure or log pressure. It is usual in climate modeling to use the pressure (or log pressure) as vertical coordinate instead of the height (altitude), as the pressure, density and altitude are linked by the hydrostatic balance :

$$\frac{\partial p}{\partial z} = -\rho g \tag{5.1}$$

And the perfect gas law :

$$p = \rho R T \tag{5.2}$$

Variations of pressure and density are related by :

$$ln(p_2) - ln(p_1) = \frac{g}{RT}(z_2 - z_1) \tag{5.3}$$

When the altitude increases (top of the plots), the pressure decreases. The quantity usually plotted are :

- The zonal wind u, i.e. the West-East component.
- The meridional wind v, i.e. the South-North component.
- The temperature T
- The streamfunctions (see Section 5.3)
- The temperature contrast, i.e. the difference with the mean temperature at the same pressure level.

During this thesis, the plots of Chapter 2 (Held Suarez) are represented as a function of the pressure p (or $\sigma = p/p_s$ with p_s the surface pressure), to be consistent with the plots in the reference paper from Held and Suarez [8] and facilitate comparisons with this paper. On the contrary, the plots of Chapter 3 (idealized Venus) are represented as a function of log pressure log(p), to be consistent with the plots used in the intercomparison study [22].
Fig. 5.1 represents the same field (the zonal-mean zonal wind u of the baseline simulation in the Held Suarez configuration) but with pressure as the y-axis on the left panel and log(pressure) on the right panel.
Positive zonal winds u correspond to winds going in the same direction as the planetary rotation : from west to east in the case of the Earth.

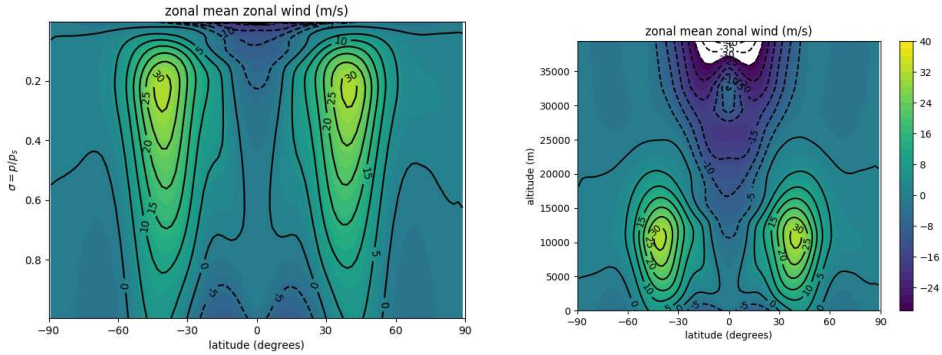

FIGURE 5.1 – zonal mean zonal wind averaged over the days 200 - 1200 of the baseline Held Suarez simulation. y-axis is either the pressure (left panel) or the log pressure (right panel).

5.2 More details on the Earth's atmospheric circulation

5.2.1 Pressure coordinates

These considerations are based on [13]. In meteorology and climate modeling, it is usual to use pressure (or log pressure) as a vertical coordinate instead of the height. This has the advantage of making the flow non divergent in pressure coordinates. Considering the perfect gas law and hydrostatic balance, one has :

$$\frac{\partial z}{\partial p} = -\frac{RT}{gp} \tag{5.4}$$

By integration, one obtains :

$$z(p) = R\int_{p}^{p_s} \frac{T}{g}\frac{dp}{p} \tag{5.5}$$

where $z(p_s) = 0$ This allows to define the thickness of an atmospheric layer, contained between the two pressure surfaces p_1 and p_2.

$$z_2 - z_1 = R\int_{p_2}^{p_1} \frac{T}{g}\frac{dp}{p} \tag{5.6}$$

Or alternatively :

$$z_2 - z_1 = \frac{R}{g}\langle T\rangle_1^2 ln(\frac{p_1}{p_2}) \tag{5.7}$$

The layer thickness depends on the temperature averaged over the layer : the layers are thicker in warmer regions (near the equator) and thinner in colder regions (near the poles).
The wind vertical component is defined in height coordinates by :

$$w = \frac{Dz}{Dt}$$

And in pressure coordinates :

$$\omega = \frac{Dp}{Dt}$$

The advective derivative is given by :

$$\frac{D}{Dt} = \frac{\partial}{\partial t} + \mathbf{u}\cdot\nabla_p + \omega\frac{\partial}{\partial p}$$

where ∇_p is the gradient operator at constant p. Using the usual derivative :

$$\omega = \frac{Dp}{Dt} = \frac{\partial p}{\partial t} + u\frac{\partial p}{\partial x} + v\frac{\partial p}{\partial y} + w\frac{\partial p}{\partial z}$$

We make the hydrostatic assumption. It becomes :

$$\omega = \frac{Dp}{Dt} = \frac{\partial p}{\partial t} + u\frac{\partial p}{\partial x} + v\frac{\partial p}{\partial y} - \rho g w \sim -\rho g w$$

As the local pressure torques and horizontal pressure advection terms are negligible in front of the vertical pressure advection terms. For the following, we will consider :

$$\omega = -\rho g w$$

5.2.2 The geostrophic balance

While the hydrostatic balance describes large scale flow balance according to the vertical, the geostrophic balance concerns the horizontal balance of large-scale flows in the case of the Earth. The atmosphere is close to the geostrophic balance in the horizontal, as pressure forces balance the Coriolis forces.
The general equation of motion is :

$$\frac{D\boldsymbol{u}}{Dt} + \frac{1}{\rho}\nabla p + \nabla\phi + f\widehat{\mathbf{z}} \times u = F \tag{5.8}$$

From a scale analysis of eq. (5.8) for large scale motion in the free atmosphere, one obtains :

$$f\widehat{\mathbf{z}} \times u + \frac{1}{\rho}\nabla p = 0 \tag{5.9}$$

The geostrophic wind, is the wind that satisfies the equation eq. (5.9) :

$$\boldsymbol{u_g} = \frac{1}{f\rho}\widehat{\boldsymbol{z}} \times \nabla p \tag{5.10}$$

The geostrophic wind is horizontal, $\boldsymbol{u_g} = (u_g, v_g, 0)$.
The Rossby number is defined by $R_o = \frac{U}{fL}$ with U and L being the motion characteristic velocity and scale and f being the Coriolis parameter, $f = 2\Omega sin(\phi)$. It represents the ratio of inertial force to Coriolis force. In the case where the Rossby number is small, the actual winds are close to geostrophic balance, meaning $\boldsymbol{u} \approx \boldsymbol{u_g}$. Translating eq. (5.10) into pressure coordinates gives :

$$\boldsymbol{u_g} = \frac{g}{f}\widehat{\boldsymbol{z}} \times \nabla_p z \tag{5.11}$$

Indeed, by considering Fig. 5.2, the pressure gradient at constant height in the z-direction is :

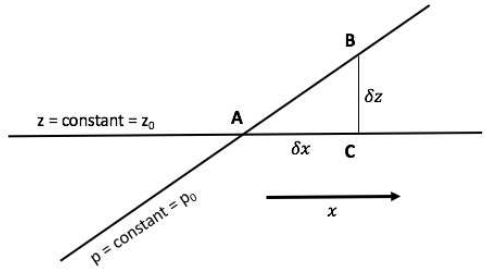

FIGURE 5.2 – Schematic representation, based on [13]

$$(\frac{\partial p}{\partial x})_z = \frac{p_c - p_0}{\delta x} \tag{5.12}$$

And the height gradient along a constant pressure surface is :

$$(\frac{\partial z}{\partial x})_p = \frac{z_B - z_0}{\delta x} \tag{5.13}$$

By considering the fact that $z_c = z_0$ and $p_B = p_0$, and using the hydrostatic balance, one obtains

$$\frac{p_c - p_0}{z_B - z_c} = -\frac{\partial p}{\partial z} = \rho g \tag{5.14}$$

which gives $p_c - p_0 = \rho g(z_B - z_0)$. We follow the same procedure in the y direction and obtain :

$$(\frac{\partial p}{\partial x})_z = \rho g(\frac{\partial z}{\partial x})_p, (\frac{\partial p}{\partial y})_z = \rho g(\frac{\partial z}{\partial y})_p \tag{5.15}$$

This leads to eq. (5.11)

5.2.3 The thermal wind relation for geostrophic balance

We derive eq. (5.11) :

$$\frac{\partial \boldsymbol{u_g}}{\partial p} = \frac{g}{f}\hat{\boldsymbol{z}} \times \nabla_p(\frac{\partial z}{\partial p}) \tag{5.16}$$

By using the perfect gas law, eq. (1.7), and the fact that the gradient is taken at constant pressure and therefore T is the only varying variable :

$$\frac{\partial \boldsymbol{u_g}}{\partial p} = -\frac{R}{fp}\hat{\boldsymbol{z}} \times \nabla_p T \tag{5.17}$$

Using the perfect gas law, eq. (1.7), to go back to height coordinates, one obtains the thermal wind relation for geostrophic balance :

$$\frac{\partial \boldsymbol{u_g}}{\partial z} = \frac{g}{fT}\hat{\boldsymbol{z}} \times \nabla_p T \tag{5.18}$$

This links wind variations according to the vertical $\frac{\partial \boldsymbol{u_g}}{\partial z}$ with the horizontal (at constant pressure) temperature gradient $\nabla_p T$. Projecting into the coordinate system, one obtains :

$$\frac{\partial u_g}{\partial z} = -\frac{\alpha}{Ttan(\phi)}\frac{\partial T}{\partial \phi} \tag{5.19}$$

with $\alpha = \frac{ag}{2\Omega} > 0$. The thermal wind relation states that for a temperature decrease toward the poles (in that case, $-\frac{1}{tan(\phi)}\frac{\partial T}{\partial \phi} > 0$ independently from the hemisphere considered), the zonal velocity of the geostrophic wind increases with altitude ($\frac{\partial u_g}{\partial z} > 0$). Inversely, an increase of temperature towards the pole leads to a decrease of the zonal velocity with altitude. The thermal wind relation does not hold at the equator and the poles, where $tan(\phi)$ tends to zero or infinity.

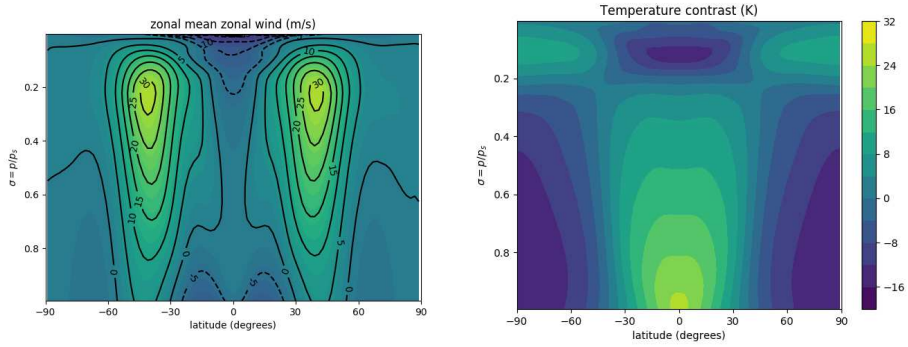

FIGURE 5.3 – zonal wind in m/s (left panel) and temperature contrast in K (right panel)

This is qualitatively quite well verified in the Held Suarez simulations, as can be seen in Fig. 5.3. For example, around 45 ° latitude, the temperature is decreasing toward the poles for

$\sigma = p/p_s < 0.2$, as the temperature contrast goes from positive values at the equator to negative values at the poles. At this latitude also, the zonal velocity is increasing with altitude until $\sigma = p/p_s < 0.2$. For $\sigma = p/p_s > 0.2$ the temperature increases toward the pole, and the zonal wind starts to decrease with increasing altitude.

5.2.4 The thermal wind relation for cyclostrophic balance

In the case of Venus, where the dominant balance is cyclostrophic and not geostrophic, a similar thermal wind relation for cyclostrophic balance can be obtained ([16]):

$$2u\frac{\partial u}{\partial \xi} = -\frac{R}{tan(\phi)}\left(\frac{\partial T}{\partial \phi}\right)_{p=constant}$$

with $\xi = -ln(\frac{p}{p_{ref}})$, p_{ref} the surface pressure, R the gas constant, T the temperature and ϕ the latitude. ξ is increasing with altitude as the pressure is decreasing. This relation links the vertical zonal wind variations with the meridional temperature gradient. As well as for the thermal wind relation for geostrophic balance, a temperature decrease toward the poles corresponds to an increase in zonal wind with altitude. Indeed, for a temperature decrease toward the poles, $-\frac{R}{tan(\phi)}(\frac{\partial T}{\partial \phi})_{p=constant} > 0$ independently from the hemisphere considered. On Venus, the velocity u is usually positive. Therefore, $\frac{\partial u}{\partial \xi} > 0$. ξ is increasing with decreasing pressure and increasing altitude, so the zonal wind will increase with altitude.
This is qualitatively quite well verified in the Venus baseline simulation, as can be seen in Figs. 3.5 and 3.6. For instance, for latitudes around 70°, the temperature is decreasing toward the poles for pressure higher (altitudes lower) than $P \approx 10^5$, and the zonal wind is increasing with altitude. For lower pressure (higher altitudes) the temperature increases toward the pole, and the zonal wind starts to decrease with increasing altitude.

5.3 Streamfunction calculation

Theory

The variations of the density in the atmosphere are significant, especially in the vertical. However, at a certain vertical level, deviations from density ρ and pressure p are usually small.
Following [23], we make the anelastic approximation and set :

$$\rho = \widetilde{\rho}(z) + \delta\rho(x, y, z, t)$$

$$p = \widetilde{p}(z) + \delta p(x, y, z, t)$$

We assume

$$|\delta\rho| << \widetilde{\rho}$$

$$\frac{\partial \widetilde{p}}{\partial z} = -g\widetilde{\rho}(z)$$

Without any approximation, the mass conservation can be written as :

$$\frac{\partial \delta\rho}{\partial t} + \nabla \cdot [(\widetilde{\rho} + \delta\rho)\mathbf{v}] = 0$$

Making the anelastic approximation, we neglect $\delta\rho$ in comparison to $\widetilde{\rho}$. In spherical coordinates, we obtain :

$$\frac{1}{acos(\phi)}\frac{\partial u}{\partial \lambda} + \frac{1}{acos(\phi)}\frac{\partial}{\partial \phi}(vcos(\phi)) + \frac{1}{\widetilde{\rho}}\frac{\partial(w\widetilde{\rho})}{\partial z} = 0 \tag{5.20}$$

We know that :

$$\frac{1}{\widetilde{\rho}}\frac{\partial(w\widetilde{\rho})}{\partial z} = -\frac{1}{\widetilde{\rho}g}\frac{\partial \omega}{\partial z} = \frac{\partial \omega}{\partial p}$$

The mass continuity equation becomes :

$$\frac{1}{acos(\phi)}\frac{\partial u}{\partial \lambda} + \frac{1}{acos(\phi)}\frac{\partial}{\partial \phi}(vcos(\phi)) + \frac{\partial \omega}{\partial p} = 0 \tag{5.21}$$

When averaging zonally and over time the mass continuity equation, one obtains :

$$\frac{1}{acos(\phi)}\frac{\partial}{\partial \phi}([\overline{v}]\, cos(\phi)) + \frac{\partial\, [\overline{\omega}]}{\partial p} = 0$$

Let $\Psi(\phi, p)$ be :

$$\Psi = \frac{2\pi a}{g} cos(\phi) \int_0^p [\overline{v}]\, dp' \tag{5.22}$$

Then,

$$[\overline{v}] = \frac{g}{2\pi a cos(\phi)} \frac{\partial \Psi}{\partial p} \tag{5.23}$$

and :

$$[\overline{\omega}] = -\frac{g}{2\pi a^2 cos(\phi)} \frac{\partial \Psi}{\partial \phi} \tag{5.24}$$

Considering the 2D zonally averaged field $\mathbf{v} = ([\overline{v}], [\overline{\omega}])$ and the 2D gradiant in spherical coordinates $\nabla\Psi = (\frac{\partial \Psi}{\partial p}, \frac{1}{a}\frac{\partial \Psi}{\partial \phi})$, we obtain :

$$\mathbf{v} \cdot \nabla \Psi = 0$$

The velocity vector $\mathbf{v}$ is perpendicular to the isocountours of Ψ.
(N.B : ω is the vertical velocity in pressure coordinate, linked to the usual vertical velocity w by : $\omega = -\rho g w$. A negative ω corresponds to a positive vertical velocity w, and uprising wind).

Streamfunction computation in the code

$$\Psi(\phi, p) = \frac{2\pi a}{g} cos(\phi) \int_0^p [\overline{v}]\, dp' \tag{5.25}$$

with $[\overline{v}] = [\overline{v}]\,(\phi, p)$ the meridional velocity averaged over time and longitude.
We discretize this integral along the vertical levels. We know the zonally and temporally averaged meridional velocity $[\overline{v}]\,(\phi, p)$ at each pressure level and latitude.

$$\Psi(\phi, p) \approx \frac{2\pi a}{g} cos(\phi) \sum_{i=0}^{i=p} [\overline{v}]\,(\Delta p)_i \tag{5.26}$$

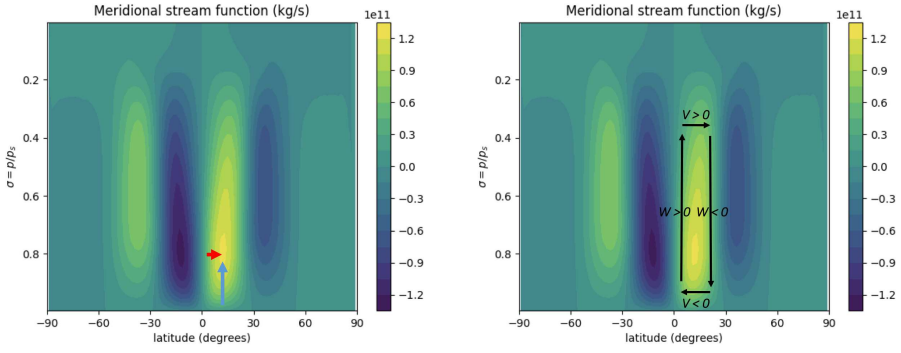

FIGURE 5.4 – Schematic representation of an Hadley cell. The plots are from our Held Suarez reference simulation.

A positive value for the stream function in the northern hemisphere corresponds to an Hadley cell, with rising motion at the equator (vertical component of the wind $w > 0$) and wind converging toward the equator close to the surface (South to North component $v < 0$). Indeed, when

considering the red arrow on Fig. 5.4 (north hemisphere, close to the equator), one has $\frac{\partial \Psi}{\partial \Phi} > 0$, as $\Delta\Psi > 0$ (increasing values of the streamfunction) and $\Delta\Phi > 0$ (increasing latitudes). Therefore, $[\overline{\omega}] < 0$. As $\omega \approx -\rho g w$ (see Section 5.2) with w the vertical motion velocity, one obtains : $[\overline{w}] > 0$. There is a rising motion near the equator.
When considering the blue arrow on 5.4 (north hemisphere, close to the surface), one has $\frac{\partial \Psi}{\partial p} < 0$, as $\Delta\Psi > 0$ (increasing values of the streamfunction) and $\Delta p < 0$ (increasing altitude, decreasing pressure). Therefore, $[\overline{v}] < 0$. This corresponds to a North-South motion in the northern hemisphere.
The same thinking holds for the other cells : a negative value of the streamfunction in the Northern hemisphere corresponds to a reverse cell, a negative value of the streamfunction in the Southern hemisphere corresponds to a Hadley cell.

5.4 Statistical analysis

5.4.1 Central Limit Theorem

As stated in [24], many non Gaussian problems can be treated as Gaussian problems, as a consequence of the Central Limit Theorem (CLT). Indeed, the Central Limit Theorem, states that for $X_1, ...X_n$ a sequence of independent and identically distributed (i.i.d.) random variables obtained from a distribution of expected value m and finite standard deviation s. Then :

$$\overline{X_n} = \frac{1}{n}(X_1 + ... + X_n) \overset{d}{\sim} N(m, \frac{s^2}{n})$$

$\overline{X_n}$ converges in distribution (when n tends to infinity) towards a normal distribution.
The main hypothesis for the CLT are :

- independent random variables : this hypothesis is not strictly verified in climate studies. Indeed, as we look at temporal series, there is always a relationship from day to day. However, this is not a problem when the data are varying quickly enough (when the correlation time is not too large).
- identically distributed random variables : this hypothesis is mostly verified.

With the CLT, one can obtain a 95 % confidence interval of the expected value m, based on the empirical mean μ and standard deviation σ of the sample.

$$I_c(m) = [\mu - q\frac{\sigma}{\sqrt{n}}, \mu + q\frac{\sigma}{\sqrt{n}}] \tag{5.27}$$

with μ and σ the sample mean and standard deviation, n the size of the sample, and q the 95% quantile, q = 1.96.

5.4.2 Bootstraping

The bootstrap is a method allowing to determine any function of a population, by using the empirical distribution. A finite sample is treated as similarly as possible to the unknown distribution [24]. This method is a resampling with replacement method. n data are drawn and this process is repeated a large number of times (n_b). One obtains n_b bootstrap samples, of size n. One calculates the statistic of interest for all the n_b bootstrap samples, and obtains the resulting frequency distribution. This method can be applied to any test statistic. It can be used to determine the mean value of a population. This method is only of interest and applicable in the case where the data to be resampled are independent. This method was implemented using random draws with Python.

5.5 Discretization of the coriolis term

In the litterature, there exist different maneers of discretizing the Coriolis term for GCMs like DYNAMICO : mainly the propositions from Thuburn (called "Thuburn" afterwards) ([9], [20]) and Gassmann (called "Gassmann" afterwards") ([7]).
The Thuburn method is implemented in DYNAMICO since the start of its development, whereas the Gassmann method is a newer one and was implemented only recently into DYNAMICO.
First, simulations were carried out with both of the methods. This allowed to discover a problem in the implementation of the Gassmann method. As the problem could not be solved before the end of the thesis, only the Thuburn method was used and is presented in the rest of the report.
The problem of the implementation in the Gassmann method was noticed by carrying simulations with positive and negative planetary rotation rate Ω. In all the simulations presented in this report, the configuration is idealized : there is no topography and the forcings are symmetric with respect to the equator. When averaging over a sufficiently long time period to get rid off the inherent variability, results should be symmetric around the equator. Therefore, changing the rotation rate of the planet from a positive value to its negative counterpart should only change the sign of the zonal winds : winds that are going from west to east ($u > 0$) in the configuration with $\Omega > 0$ should go from east to west ($u < 0$), and vice versa, as shown schematically in Fig. 5.5.

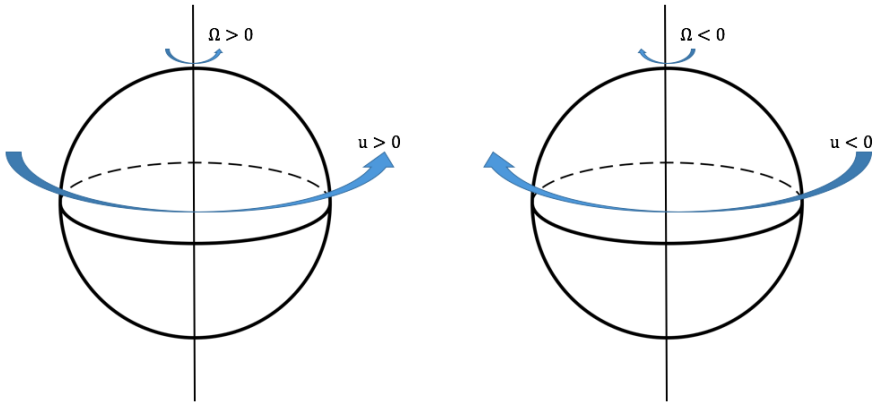

FIGURE 5.5 – Schematic representation of the effect of the rotation rate sign on the winds

When not specified, Ω was taken positive for simplicity, even if Venus is counter rotating. This does not impact the results except for the sign. As on Earth, $\Omega > 0$, it is a convention and a custom to have $u > 0$ when going into the same direction as the planetary rotation.
The normalized AAM is plotted on Fig. 5.6 for four different simulations : with $\Omega > 0$ or < 0 and the two variants of the discretization of the Coriolis force : Thuburn and Gassmann. One can see that the two simulations with the Gassmann method lead to very different results, whereas the two simulations using the Thuburn method have really similar results.
This shows a problem in the implementation of the Gassmann method, as it should give identical results (up to truncation and statistical errors) in both cases $\Omega > 0$ or $\Omega < 0$.

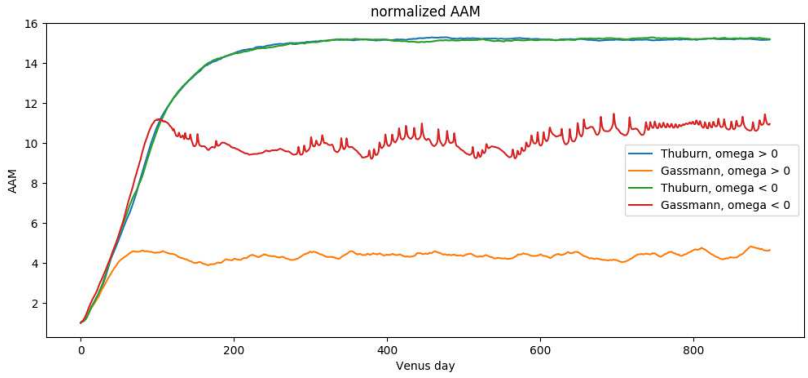

FIGURE 5.6 – normalized AAM of four different simulations

5.6 Instability in Venus simulations

Baseline simulation

An instability was found in some Venus simulations. The meridional velocity v is found to oscillate between positive and negative values between each vertical level for the levels located between approximately 10^7 and 10^5 Pa. This is visible in the plots of the meridional velocity averaged zonally in Fig. 5.7, and in Fig. 5.8, where the meridional velocity at particular latitudes was plotted as a function of the pressure (vertical level).

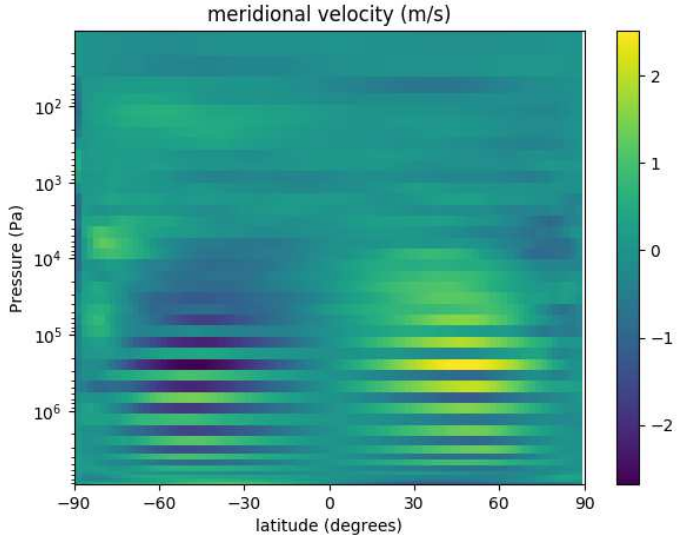

FIGURE 5.7 – meridional velocity (m/s), averaged zonally and over Venus days 130 and 150

A purely numerical instability ? Influence of the vertical levels

One wanted to know if this instability found on the baseline runs was due to a physical reason (if the amount of vertical levels used to represent the flow is not sufficient for example) or if it

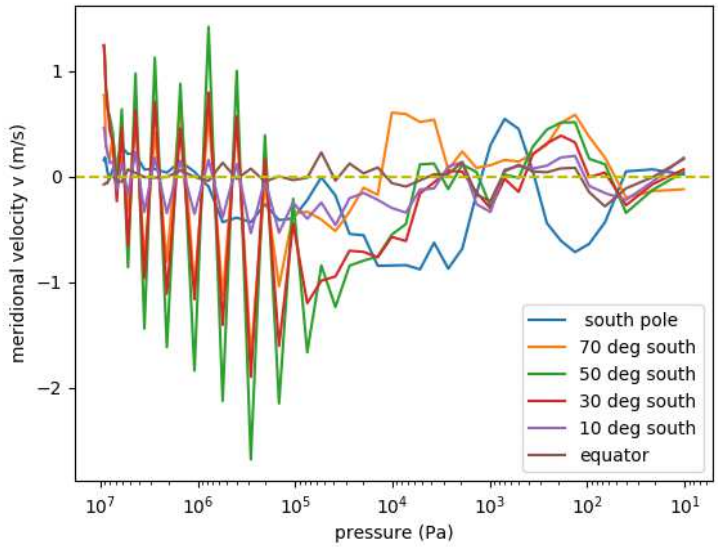

FIGURE 5.8 – meridional velocity (m/s), averaged zonally and over Venus days 130 and 150 at several latitudes

was due to a numerical instability. To check this hypothesis, the amount of vertical levels was doubled. The instability remained present, with strong oscillations, as one can see in Fig. 5.9. This tends to suggest that the origin of the instability is numerical.
The amount of vertical level was also decreased, and the instability also remained present.

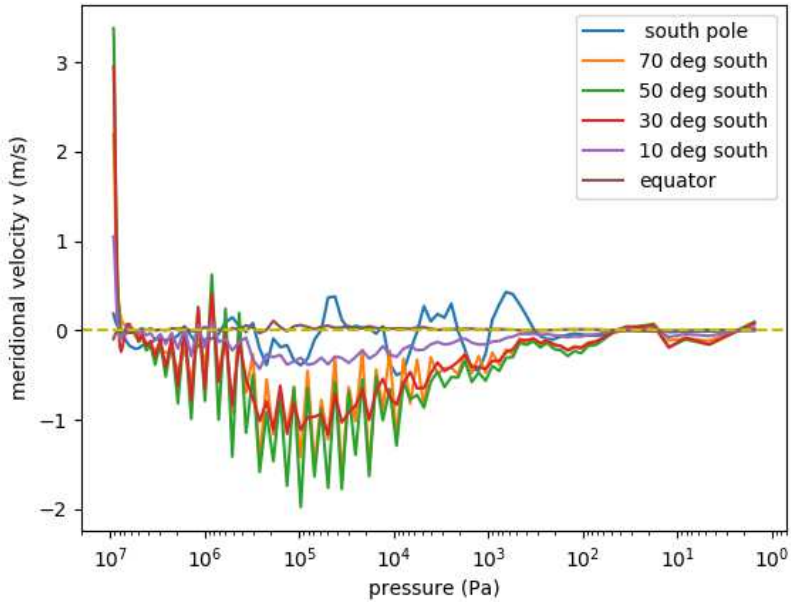

FIGURE 5.9 – meridional velocity (m/s) at different latitudes for a simulation with two times more vertical levels than the baseline simulation

Instability in other GCM simulations

However, this instability is not characteristic from DYNAMICO, as it is seen in other GCM simulations, when modeling the Venusian atmosphere.

Indeed, the instability was also found in one of the two simulations carried by S. Lebonnois using the other LMD dynamical core LMDZ. One of the simulation is using a constant Cp for the atmosphere, while the other is taking into account the fact that Cp varies with the temperature. All the simulations carried out during this work with DYNAMICO consider that Cp is a constant. The instability is much probably not directly related to the fact that Cp is taken as a constant or not, as the general circulation obtained in both cases differ widely. One can see the different general circulation obtained on Fig. 5.10 and Fig. 5.12.

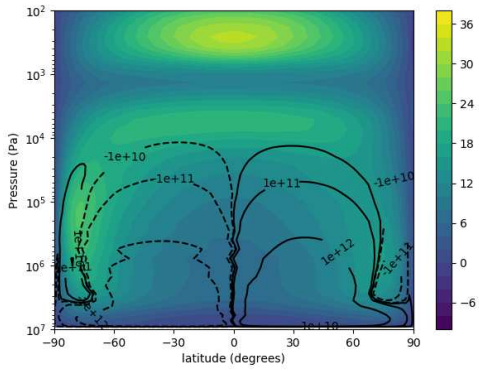

FIGURE 5.10 – General circulation. The zonal velocity is represented in colors, the meridional circulation (streamlines) in black contours. Data is averaged between VD = 96 -106. Case with Cp taken as a constant.

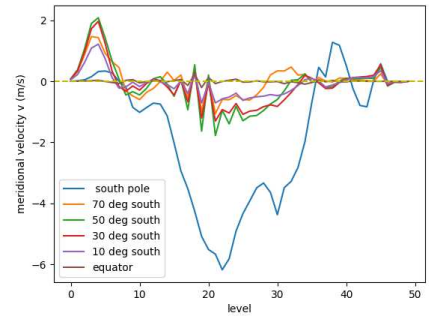

FIGURE 5.11 – meridional velocity averaged zonally between VD = 96-106. Case with Cp taken as a constant.

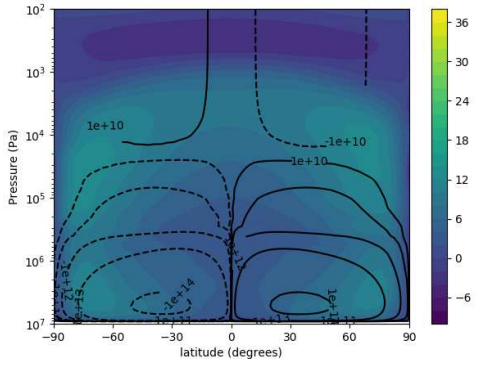

FIGURE 5.12 – General circulation. The zonal velocity is represented in colors, the meridional circulation (streamlines) in black contours. Data is averaged between VD = 96 -106.Case with Cp varying with temperature.

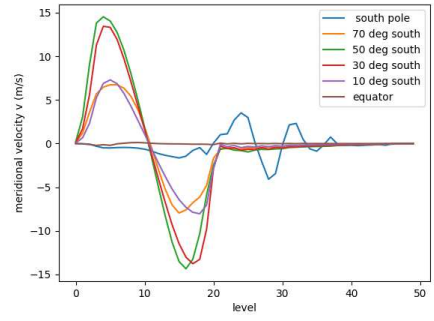

FIGURE 5.13 – meridional velocity averaged zonally between VD = 96-106. Case with Cp varying with temperature.

This instability is also visible in some other GCM in the results of the Venus intercomparison study [22]. The meridional velocity v are not plotted but the streamfunctions (shown in Fig. 5.14) have a spurious oscillating feature along the vertical, which tends to indicate fluctuations in the meridional velocity.

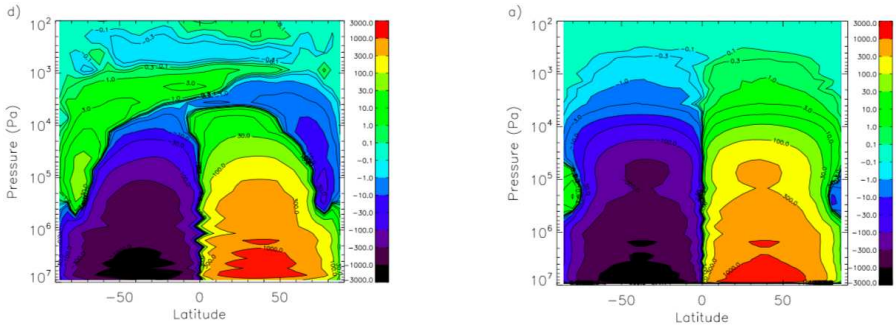

FIGURE 5.14 – zonally and temporally averaged streamfunction of the CSSR and Oxford GCM in the baseline configuration of the intercomparison study [22].

Influence of the dissipation

Several simulations with DYNAMICO were carried out, by varying the dissipation coefficients. In some cases the instability does appear and does not in some other. No "easy" relationship with the dissipation coefficient could be seen. For example, the instability appeared in simulations with a medium dissipation coefficient, and not in simulations with a high or low dissipation coefficient. Between these simulations, the general circulation differed widely. Therefore it suggests that the instability is favoured by certain types of circulation (generated by different dissipation coefficients).
Due to a lack of time, this instability could not be furthered investigated.

Bibliography

[1] Conservation du moment cinetique dans le modele de circulation generale du lmd. http://lmdz.lmd.jussieu.fr/le-coin-des-developpeurs/notes-techniques/ressources/conserv.pdf. Accessed: 2019-06-11.

[2] DYNAMICO status and outlook. https://www.esiwace.eu/events/5th-enes-hpc-workshop/presentations/dubos-dynamico. Accessed: 2019-07-21.

[3] T. Imamura P. Read D. Luz A. Sanchez Lavega, S. Lebonnois. *The atmospheric Dynamics of Venus*. 2017.

[4] A Staniforth AA White, BJ Hoskins I Roulstone. Consistent approximate models of the global atmosphere: shallow, deep, hydrostatic, quasi-hydrostatic and non-hydrostatic. *QUARTERLY JOURNAL OF THE ROYAL METEOROLOGICAL SOCIETY*, (131 (609)):2081–2107, 2005.

[5] T Dubos, S Dubey, M Tort, R Mittal, Y Meurdesoif, and F Hourdin. DYNAMICO-1.0, an icosahedral hydrostatic dynamical core designed for consistency and versatility. *Geoscientific Model Development*, 8(10):3131–3150, 2015.

[6] K. Weickmann Egger, J. and K.-P. Hoinka. ANGULAR MOMENTUM IN THE GLOBAL ATMOSPHERIC CIRCULATION. *Rev. Geophys.*, (45), 2007.

[7] Almut Gassmann. Discretization of generalized coriolis and friction terms on the deformed hexagonal c-grid. *Quarterly Journal of the Royal Meteorological Society*, 144(716):2038–2053, 2018.

[8] Suarez Held. A Proposal for the Intercomparison of the Dynamical Cores of Atmospheric General Circulation Models. *Bulletin of the American Meteorological Society*, 1994.

[9] W.C. Skamarock J.B. Klemp J. Thuburn, T.D. Ringler. Numerical representation of geostrophic modes on arbitrarily structured c-grids. *Journal of Computational Physics*, 228(22):8321–8335, 2009.

[10] C. Covey A. Grossman H. Parish G. Schubert R. Walterscheid P. Lauritzen Lebonnois, S. and C. Jablonowski. Angular momentum budget in General Circulation Models of superrotating atmospheres: A critical diagnostic. *J. Geophys.Res.*, (117), 2012.

[11] Christopher Lee. *Modelling of the atmosphere of Venus*. PhD thesis, University of Oxford, 2006.

[12] Christopher Lee, Stephen R Lewis, and Peter L Read. Superrotation in a venus general circulation model. *Journal of Geophysical Research: Planets*, 112(E4), 2007.

[13] J. Marshall and R.A. Plumb. *Atmosphere, Ocean and Climate Dynamics: An Introductory Text*. International Geophysics. Elsevier Science, 1969.

[14] Peter H. Lauritzen Christiane Jablonowski Mark A. Taylor Ramachandran D. Nair. *Numerical Techniques for Global Atmospheric Models*. Springer-Verlag, Berlin Heidelberg, 2011.

[15] Andrew Orr. Thomas t. warner, 2011. numerical weather and climate prediction, cambridge university press, cambridge, uk. isbn: 978-0-521-51389-0. hardback, 526 pp. *Meteorological Applications*, 19(3):E1–E1, 2012.

[16] Arianna Piccialli. *Cyclostrophic wind in the mesosphere of Venus from Venus Expressobservations*. PhD thesis, Technischen Universität Carolo-Wilhelminazu Braunschweig, 2010.

[17] Agustín Sanchez-Lavega, Sébastien Lebonnois, Takeshi Imamura, Peter L. Read, and David Luz. The Atmospheric Dynamics of Venus. *Space Science Reviews*, 212(3-4):1541 – 1616, November 2017.

[18] A. Seiff, J.T. Schofield, A.J. Kliore, F.W. Taylor, S.S. Limaye, H.E. Revercomb, L.A. Sromovsky, V.V. Kerzhanovich, V.I. Moroz, and M.Ya. Marov. Models of the structure of the atmosphere of venus from the surface to 100 kilometers altitude. *Advances in Space Research*, 5(11):3 – 58, 1985.

[19] F. Taylor and D. Grinspoon. Climate evolution of venus. *Journal of Geophysical Research: Planets*, 114(E9), 2009.

[20] J.B. Klemp W.C. Skamarock T.D. Ringler, J. Thuburn. A unified approach to energy conservation and potential vorticity dynamics for arbitrarily-structured c-grids. *Journal of Computational Physics*, 229(9):3065–3090, 2010.

[21] J. Thuburn. Some conservation issues for the dynamical cores of nwp and climate models. *Journal of Computational Physics*, 227(7):3715–3730, 2008.

[22] S. Lebonnois · C. Lee · M. Yamamoto · J. Dawson · S. R. Lewis · J. Mendonca · P. L. Read · H. Parish · G. Schubert · L. Bengtsson · D. Grinspoon · S. Limaye · H. Schmidt · H. Svedhem · D. Titov. *A Comparative Analysis of Simplified General Circulation Models of Venus Atmosphere*. 2012.

[23] G. K. Vallis. *Atmospheric and Oceanic Fluid Dynamics*. Cambridge University Press, Cambridge, U.K., 2006.

[24] D. Wilks. *Statistical Methods in the Atmospheric Sciences,*. 2005.

[25] D. Williamson. The Evolution of Dynamical Cores for Global Atmospheric Models. *Journal of the Meteorological Society of Japan*, (85B):241–269, 2007.

[26] Masaru Yamamoto and Masaaki Takahashi. General circulation driven by baroclinic forcing due to cloud layer heating: Significance of planetary rotation and polar eddy heat transport. *Journal of Geophysical Research: Planets*, 121(4):558–573, 2016.

[27] Masaru Yamamoto and Masaaki Takahashi. Effects of polar indirect circulation on superrotation and multiple equilibrium in long-term agcm experiments with an idealized venus-like forcing: Sensitivity to horizontal resolution and initial condition. *Journal of Geophysical Research: Planets*, 123(3):708–728, 2018.